



Calhoun: The NPS Institutional Archive DSpace Repository

Theses and Dissertations

1. Thesis and Dissertation Collection, all items

1990-09

Thermal and mechanical fatigue of 6061 Al - P100 Gr metal matrix composite

Hansen, Robert C.

Monterey, California. Naval Postgraduate School

<http://hdl.handle.net/10945/37562>

This publication is a work of the U.S. Government as defined in Title 17, United States Code, Section 101. Copyright protection is not available for this work in the United States.

Downloaded from NPS Archive: Calhoun



<http://www.nps.edu/library>

Calhoun is the Naval Postgraduate School's public access digital repository for research materials and institutional publications created by the NPS community.

Calhoun is named for Professor of Mathematics Guy K. Calhoun, NPS's first appointed -- and published -- scholarly author.

Dudley Knox Library / Naval Postgraduate School
411 Dyer Road / 1 University Circle
Monterey, California USA 93943

(2)

NAVAL POSTGRADUATE SCHOOL

Monterey, California

AD-A238 795



DTIC
SELECTED
JUL 23 1991
S B D

THESIS

Thermal and mechanical fatigue of laminated
6061 Al - P100 Gr metal matrix composite.

by

Robert C. Hansen

September, 1990

Thesis Advisor:
Co-Advisor:

Indranath Dutta
Shantanu Mitra

Approved for public release; distribution is unlimited.

91-05583



30

10

111

UNCLASSIFIED

SECURITY CLASSIFICATION OF THIS PAGE

REPORT DOCUMENTATION PAGE

1a. REPORT SECURITY CLASSIFICATION UNCLASSIFIED		1b RESTRICTIVE MARKINGS	
2a. SECURITY CLASSIFICATION AUTHORITY		3 DISTRIBUTION/AVAILABILITY OF REPORT Approved for public release; distribution is unlimited.	
2b. DECLASSIFICATION/DOWNGRADING SCHEDULE			
4 PERFORMING ORGANIZATION REPORT NUMBER(S)		5 MONITORING ORGANIZATION REPORT NUMBER(S)	
6a. NAME OF PERFORMING ORGANIZATION Naval Postgraduate School	6b OFFICE SYMBOL (If applicable) 69	7a. NAME OF MONITORING ORGANIZATION Naval Postgraduate School	
6c. ADDRESS (City, State, and ZIP Code) Monterey, CA 93943-5000		7b ADDRESS (City, State, and ZIP Code) Monterey, CA 93943-5000	
8a. NAME OF FUNDING/SPONSORING ORGANIZATION	8b OFFICE SYMBOL (If applicable)	9. PROCUREMENT INSTRUMENT IDENTIFICATION NUMBER	
8c. ADDRESS (City, State, and ZIP Code)		10. SOURCE OF FUNDING NUMBERS	
		Program Element No.	Project No.
		Task No.	Work Unit Accession Number
11. TITLE (Include Security Classification) THERMAL AND MECHANICAL FATIGUE OF LAMINATED 6061 AL - P100 GR METAL MATIX COMPOSITE.			
12. PERSONAL AUTHOR(S) Hansen, Robert, C.			
13a. TYPE OF REPORT Master's Thesis	13b. TIME COVERED From To	14. DATE OF REPORT (year, month, day) September 1990	15. PAGE COUNT 74
16. SUPPLEMENTARY NOTATION The views expressed in this thesis are those of the author and do not reflect the official policy or position of the Department of Defense or the U.S. Government.			
17. COSATI CODES		18. SUBJECT TERMS (continue on reverse if necessary and identify by block number) aluminum-graphite composite, bend fatigue, thermal fatigue	
FIELD	GROUP	SUBGROUP	
19. ABSTRACT (continue on reverse if necessary and identify by block number) Aluminum-Graphite (6061 Al/P100 Thoral fiber) composite material, with [0/90] cross plies and 40% fiber volume, was tested under thermal and mechanical cyclic loading. Initial thermal cycling experiments of a diffusion bonded, 11 ply composite showed crack nucleation at regions of poor liquid metal infiltration in the fiber tows when heated from room temperature (RT) to 640 C, after one cycle, as seen using the edge replication technique. Similar experiments from RT to 100 C did not show similar damage after 120 cycles. Dilatometry experiments showed the existence of thermal residual strain after one heating cycle between (a) RT to 100 C and (b) RT to 640 C. Thermal strain hysteresis was also observed in both temperature ranges. These effects have been explained using matrix time dependent plasticity and residual stress concepts. It was found that the residual stresses existing at RT after fabrication, due to differences in coefficient of thermal expansion of aluminum and graphite, seriously effected the subsequent strain behavior. Transmission electron microscopy revealed poor wetting of the graphite fibers due to the lack of the standard Titanium Boride coating used in these composites. Finally, a different type of fabricated composite, viz. a cast, three ply composite of the same matrix and reinforcement, was studied in bend fatigue loading. Two different configurations, along with the monolithic matrix material, were tested in the range of 65 to 95 percent of their respective ultimate bending strengths (URS). Crack initiation and propagation studies, along with S-N curves, are also presented. Fiber orientation was found to play a significant role in fatigue strength, and crack propagation.			
20. DISTRIBUTION/AVAILABILITY OF ABSTRACT <input checked="" type="checkbox"/> UNCLASSIFIED/UNLIMITED <input type="checkbox"/> SAME AS REPORT <input type="checkbox"/> DTIC USERS		21. ABSTRACT SECURITY CLASSIFICATION Unclassified	
22a. NAME OF RESPONSIBLE INDIVIDUAL Indranath Dutta, Professor		22b. TELEPHONE (Include Area code) (408) 646-2681	22c. OFFICE SYMBOL 69DU

Approved for public release; distribution is unlimited.

Thermal and mechanical fatigue
of 6061 Al - P100 Gr metal matrix composite.

by

Robert C. Hansen
Lieutenant, United States Navy
B.S., University of Missouri-Columbia

Submitted in partial fulfillment
of the requirements for the degree of

MASTER OF SCIENCE IN MECHANICAL ENGINEERING

from the

NAVAL POSTGRADUATE SCHOOL
September 1990

Author:

Robert C. Hansen

Approved by:

Indranath Dutta, Thesis Advisor

Shantanu Mitra, Thesis Co-Advisor

Anthony J. Healey, Chairman

Department of Mechanical Engineering

ABSTRACT

Aluminum-Graphite (6061 Al/P100 Thorne fiber) composite material, with [0/90] cross plies and 40% fiber volume, was tested under thermal and mechanical cyclic loading. Initial thermal cycling experiments of a diffusion bonded, 11 ply composite showed crack nucleation at regions of poor liquid metal infiltration in the fiber tows when heated from room temperature (RT) to 540 °C after one cycle, as seen using the edge replica technique. Similar experiments from RT to 100 °C did not show similar damage after 120 cycles. Dilatometry experiments showed the existence of thermal residual strain after the first heating cycle between (a) RT to 100 °C and (b) RT to 540 °C. Thermal strain hysteresis was also observed in both temperature ranges. These effects have been explained using matrix time dependent plasticity and residual stress concepts. It was found that the residual stresses existing at RT after fabrication, due to differences in coefficient of thermal expansion of aluminum and graphite, seriously effected the subsequent strain behavior. Transmission electron microscopy revealed poor wetting of the graphite fibers due to the lack of the standard TiB₂ coating used in these composites. Finally, a different type of fabricated composite, viz., a cast, three ply composite of the same matrix and reinforcement, was studied in bend fatigue loading. Two different sample configurations, along with the monolithic matrix material, were tested in the range of 65 to 95 percent of their respective ultimate bending strengths (UBS). Crack initiation and propagation

studies, along with S-N curves, are also presented. Fiber orientation was found to play a significant role in fatigue strength, and crack propagation.

Accession For	
NTIS GRA&I	<input checked="" type="checkbox"/>
DTIC TAB	<input type="checkbox"/>
Unannounced	<input type="checkbox"/>
Justification	
By _____	
Distribution/	
Availability Codes	
Dist	Avail and/or Special
A-1	

TABLE OF CONTENTS

I. INTRODUCTION	1
II. LITERATURE SURVEY	5
A. THERMAL STRESSES OF MMC	5
B. MECHANICAL FATIGUE OF MMC	10
C. RESEARCH OBJECTIVES AND OVERVIEW	13
III. EXPERIMENTAL EQUIPMENT AND TECHNIQUES	15
A. THERMAL CYCLING	15
B. FATIGUE	18
IV. EXPERIMENTAL PROCEDURES	21
A. MATERIALS	21
B. PROCEDURES	22
V. RESULTS AND DISCUSSION	27
A. THERMAL CYCLING	27
B. FATIGUE	42

VI. SUMMARY	56
APPENDIX A	58
APPENDIX B	62
LIST OF REFERENCES	64
INITIAL DISTRIBUTION LIST	66

I. INTRODUCTION

Metal matrix composites (**MMCs**) are an attractive class of materials that offer certain advantages over conventional, monolithic materials. The matrix of an MMC can transfer loads to the reinforcing fibers, and will generally be softer than and have a relatively lower modulus of elasticity than the fibers. By combining a low density, relatively ductile matrix with a relatively strong continuous fiber, an MMC with a high strength-to-weight ratio and a high modulus-to-weight ratio can be produced [Ref. 1].

Aluminum-graphite (Al-Gr) continuous fiber reinforced laminate MMCs have numerous potential applications not only where low density, and high stiffness are required, but also where excellent thermal conductivity is needed. These MMCs are being developed primarily for use in aircraft and space vehicles where modern alloys and monoliths fail to fulfill design requirements [Ref. 2]. Due to the thermal conductivity properties of aluminum and graphite, the coefficient of thermal expansion (**CTE**) of Al-Gr composites in temperature fluctuating conditions is important. This behavior (**CTE**) is effected by a number of factors like, fiber orientation, thermal processing, residual stresses, etc., of which the thermal residual stresses in the matrix play an important role. These residual stresses can reach large values in the matrix, along the fiber direction, due to large differences in the individual CTEs of aluminum and graphite. The residual stresses are further compounded by both longitudinal and transverse ply constraints.

Besides these residual stresses, the integrity of the interfacial bond between aluminum and graphite is also important. The quality of the interface is a function of "wetting" of

the graphite fibers by liquid aluminum during the manufacturing process of the composite [Ref. 3]. Laminate MMCs are manufactured primarily by diffusion bonding of individual laminae, or by casting. The fibers are consolidated into tows which are infiltrated by the liquid metal matrix.

Enhancement of wetting of graphite fibers in Al-Gr MMCs is accomplished by depositing a thin coat of titanium and boron onto the fiber tows using a process called chemical vapor deposition (CVD). A TiB_2 layer is then formed, which promotes good wetting when the molten aluminum comes into contact with the fibers. For the diffusion bonding process, these infiltrated, titanium boride coated fiber tows are placed between foils of aluminum, heated to approximately $550\text{ }^{\circ}\text{C}$ (below the melting temperature of aluminum) and compressed at a high pressure for a specified length of time to promote a good metallurgical bond between the aluminum matrix from adjacent laminae. [Ref. 3]

The number of plies in an MMC is equal to the number of continuous fiber layers. The fiber layers may or may not be unidirectional. Fiber direction is measured with respect to the longitudinal axis. Figure 1 illustrates a three ply [0/90] MMC laminate; [0/90] indicates alternating layers of plies oriented 0 and 90 degrees with respect to the longitudinal axis of the sample.

The Naval Weapons Support Center, Crane, Indiana is considering using [0/90] cross plied Al-Gr MMCs (6061 Al/P100 Thormel) with 40% fiber volume as the mounting frame for electronic modules because of its low-density, high-stiffness, and high thermal conductivity due to the high fiber volume. The high thermal conductivity is the most important feature since heat removal from electronic components in confined areas, such

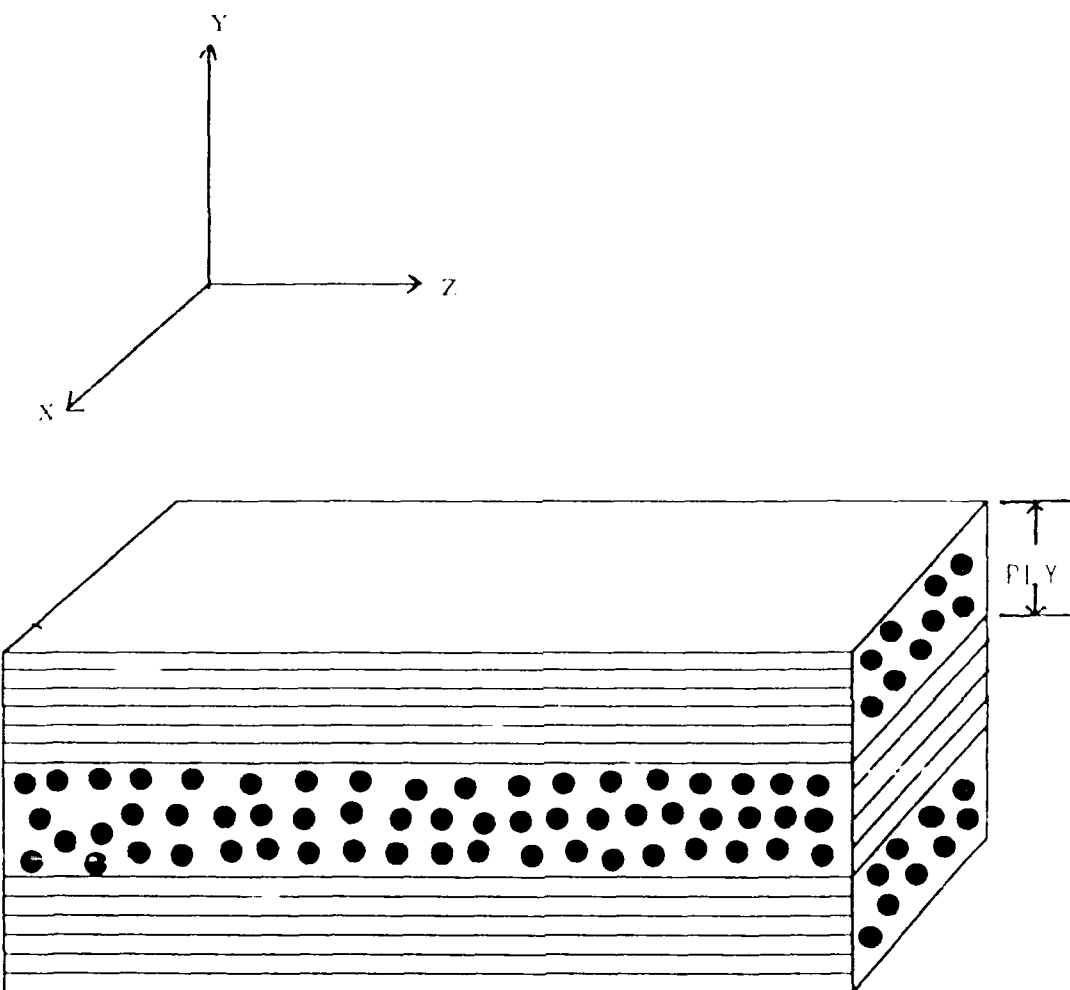


Figure 1: Illustration of a three ply [0/90] metal matrix composite laminate. The Z axis is the longitudinal axis and the X axis is the transverse axis.

as aircraft electronic compartments, is a limiting design criteria for aircraft weapon systems. Consequently, the CTE of the entire composite, over various temperature ranges, and the response to mechanical fatigue loading are of critical importance. The work described in this thesis involves investigating the effect temperature ranges, thermal treatments, and mechanical cyclic loading has on the failure modes and mechanisms of [0/90] cross plied 6061 Al/P100 Gr MMCs.

II. LITERATURE SURVEY

A. THERMAL STRESSES OF MMC

1. Thermal Residual Stresses

The CTE of the aluminum matrix is generally much greater than the CTE of the reinforcing graphite fiber. In the composites used in this study, the CTE values are as follows:

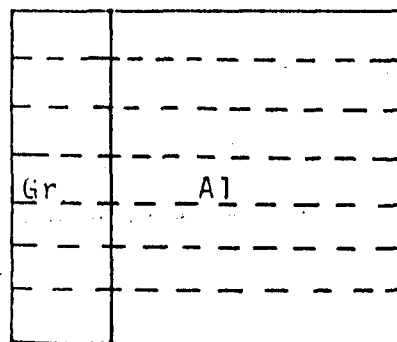
• 6061 aluminum, $\alpha_{Al} = 21.6 \times 10^{-6}/^{\circ}C$

• P100 graphite, $\alpha_{Gr, long.} = -0.9 \times 10^{-6}/^{\circ}C$

Because of the large difference in CTE, large, residual thermal stresses develop after cooling from the manufacturing temperature. Figure 2 shows a conceptual thermal excursion undergone by the MMC when manufactured [Ref. 4]. Large, longitudinal, tensile residual stresses are generated in the matrix due to this effect.

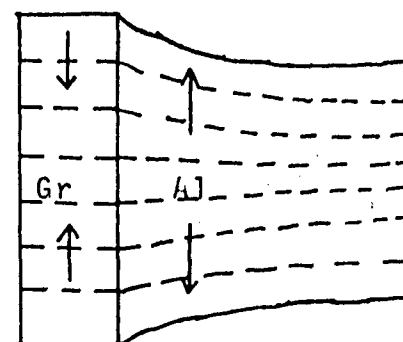
In Al-Gr MMCs, the large difference in CTE occurs in the longitudinal direction of the fiber only, because of the anisotropy of the graphite fiber's CTE; therefore, one may expect the residual stresses in the transverse direction of unidirectional MMC not to be as significant as those in the longitudinal direction. However, research presented by S. Tsai et al. [Ref. 5], using 201 Al/P50 MMC, shows that the residual stresses in the transverse direction, which are also tensile, are significant despite no significant difference in the CTE. This was attributed to Poisson's effect.

Fabrication
Temperature



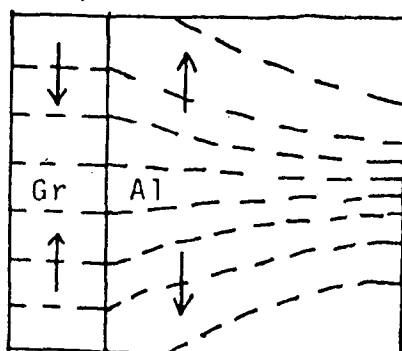
(a)

Room
Temperature



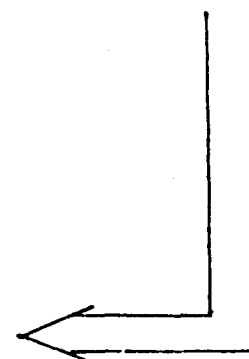
(b)

Room
Temperature



(cut to shape)

(c)



→ = Longitudinal stress

- - - = Schematic of lattice planes, showing distortion due to residual stresses induced on cooling.

Figure 2: A conceptual thermal excursion undergone by a small section of the matrix adjacent to a fiber in an MMC during manufacturing. Figure c is after cutting to make fiber ends and matrix flush. [Ref. 4]

Tsai et al. [Ref. 5] also found that subjecting the composite to a cryogenic treatment relieved most of the residual stresses induced by cooling from the manufacturing temperature. By cooling the composite to liquid nitrogen temperature, plastic flow is induced in the matrix, thereby relieving some of the stresses. Once the composite is heated back to room temperature, most of the residual stresses are then thermally relieved.

Park [Ref. 6] used X-ray techniques to measure the residual stresses in 6061 Al/P100 Gr unidirectional, single ply, as-fabricated MMCs and found them to be tensile in a direction parallel to the fibers. When the composite was quenched in liquid nitrogen the residual stresses at room temperature were found to be compressive.

Besides matrix yielding due to overloading, these residual stresses are capable of inducing creep type relaxation in the matrix at elevated temperatures. This has been recognized by several workers, including Koss and Copley [Ref.7], Garmong [Ref. 8], and Wolff et al. [Ref. 9], who indicated that heating and cooling rates determine thermal strain response of MMCs. Heat treating an aluminum matrix composite to an intermediate temperature (i.e., moderate to high homologous temperature) would then induce creep in the matrix and reduce or eliminate any residual stresses. When the composite's temperature is reduced back to room temperature, the change in temperature is small enough not to induce any significant residual stresses, since

$$RESIDUAL\ STRESS \propto \Delta\alpha\Delta T \quad (1)$$

To understand the effect the difference in CTE has on thermal residual stresses of multi-layer laminate MMCs, one must first examine a lamina, (i.e., one layer of the composite). M. Kural and B. Min [Ref. 2] show that, in general, the strain response of a laminate to residual stress is similar to a lamina's. In cross plied composites, the transverse plies, which are perpendicular to the Z axis (figure 1), also affect the residual stresses by applying an additional constraint to the longitudinal ply. An additional contribution is thus made to the tensile residual stresses in the longitudinal layer when cooled from fabrication temperatures. Although the $\Delta\alpha$ in the fiber's radial direction is very small, the existence of transverse residual stresses (as measured by Tsai et al. [Ref. 5]) ensures larger tensile residual stresses in the Z direction (figure 1) of the longitudinal ply. In this study, the value of the stress in the Z direction is important due to its effects on the longitudinal strain behavior over the entire composite, and since it is the axis of strain measurement in the dilatometer.

Since the resultant stresses at room temperature of cross ply composites are tensile, the maximum tensile load the composite can handle is reduced.

2. Effects of Thermal Cycling

Thermal stresses, thermal strains, and mechanical properties of MMCs are greatly effected by thermal cycling, such as the heating and cooling of electronic components, and by various environmental effects.

Dries and Tompkins [Ref. 10] studied unidirectional P100 Gr/6061 Al and found that after the first cycle, between -250 °F and 250 °F, a large, tensile residual strain existed, but disappeared during subsequent cycling. Cycling from room temperature to

250 °F produced a compressive residual strain after the first cycle. Thermal strain hysteresis continually existed during cycling but kept decreasing due to matrix strengthening. These authors [Ref. 10] argued that hysteresis was due to the fact that the magnitude of the thermal stresses created during thermal cycling exceeded the elastic limits of the matrix alloy (i.e., plastic yielding occurs). Dries and Tompkins [Ref. 11] later observed that post-consolidation thermal processing, which consists of solution heat treatment, water quench to room temperature, aging to increase the matrix's elastic limit, then quenching in liquid nitrogen, eliminated the thermal strain hysteresis in unidirectional, and low angle ply laminates. This process was tested on different composites but eliminated the strain hysteresis in Al-Gr MMCs only. The increase in matrix yield strength, with aging, prevented any plastic strain, and according to Dries and Tompkins [Ref. 11], did not give any hysteresis in low angle laminates after processing. Wolff et al. [Ref. 9] also found the primary cause of hysteresis to be matrix yielding due to residual stresses during cycling.

The effects of thermal cycling on residual stresses in Al-Gr MMCs is dependent on the temperature range. Thermal cycling produces micro-damage at the fiber/matrix interface, due to the large residual stresses. This micro-damage allows some relaxation of the residual stresses. The greater the temperature, the more the matrix relaxation.

Khan [Ref. 12] showed that ultimate tensile strength (UTS) of unidirectional, diffusion bonded Al-Gr composites is not affected by thermal exposure up to 500 °C; above this temperature the UTS decreased significantly. The loss in strength is attributed to the formation of aluminum carbide (Al_4C_3) above 500 °C at the fiber/matrix interface.

The Al_4C_3 formation observed by Khan was between amorphous carbon and aluminum without a titanium boride barrier. Khan also showed that thermal cycling of the composite between 20 °C and 500 °C causes a reduction of about 18% in UTS during the first 10 cycles with no appreciable degradation beyond this. Olsen and Tompkins [Ref. 13] have produced similar results in aluminum-boron composites. Results presented by Dries and Tompkins [Ref. 10] show that the UTS and stiffness of the diffusion bonded Al-Gr composites increased with thermal cycling; this contradicts Khan's data. Dries and Tompkins attributed the increase in UTS of the unidirectional composites to the aging of the aluminum matrix alloy during thermal cycling.

From previous research, it is evident that the need to study the effects of thermal cycling on cross plied MMCs exists, and is the subject of investigation in this study.

B. MECHANICAL FATIGUE OF MMC

Fatigue failures of metals occur in the following sequence:

- Crack initiation - generally at a free surface due to intrusions and extrusions [Ref. 14].
- Crack propagation - dependent on material, crack tip radius, applied stress, and crack tip blunters and dividers.
- Catastrophic failure - occurs when the crack has grown to a point where the remaining cross section is unable to support the load.

Three primary factors must be present to cause this sequence to occur.

- A sufficiently high tensile stress.

- A relatively large fluctuation in the applied stress.
- A sufficient number of cycles of the applied stress.

Other factors that can effect the fatigue sequence are stress concentration, residual stresses, corrosion, temperature, and especially, surface finish. Specimens that have smooth, highly polished surfaces have shown the highest fatigue lives. This is due to the removal of possible crack initiation sites associated with rough surfaces.

The relationship between defects and material response of monolithic material is adequately predicted by fracture mechanics. However, in laminate MMCs, fatigue failure is controlled by the matrix and fiber material, by constraints imposed by the undamaged plies on the damaged plies, and by the orientation of the damaged plies with respect to the load [Ref. 15]. Because multiple failure mechanisms are involved, prediction of crack initiation and propagation in MMCs is much more complex.

Crack initiation: Tension-tension fatigue tests have shown that there are many sources for crack initiation in MMC. The most common source is at the fiber flaws/breaks which occur during manufacturing [Ref. 16, 19]. This means that cracks are initiated early in life, at these defects, and most of the fatigue life is thus spent in the crack propagation mode. Other factors effecting initiation include large, residual stresses in the matrix, weak interfaces, and precipitates in the interfacial zone [Ref. 16, 17]. Unlike tension-tension fatigue where fibers, interface, and matrix are subjected to the same applied stress throughout the cross-section, bend fatigue tests are different. Bend fatigue crack initiation can occur at a free surface, at imperfections between the matrix and fiber

due to poor interfaces, poor wetting, or cracked fibers, or at points of maximum tensile stress (i.e., furthest away from the neutral axis on the tension side).

Crack propagation can do one of the following:

- Be blunted by the fiber/matrix interface.
- Run through the matrix to a fiber and propagate along the fiber/matrix interface (along the fiber length, i.e., debonding) or around the fiber. The crack then continues through the matrix on the other side.
- Run through the matrix to a fiber, fracture the fiber and continue through the matrix on the other side. This process depends on the reinforcing fiber.

This clearly shows that fiber/matrix interfaces and fiber strength play major roles in the fatigue of MMCs. Fatigue failure in Al-Gr MMCs has been shown to be a "... process of crack initiation at points of cavities and inclusions, leading to crack propagation along the previously broken fibers," that exist from manufacturing flaws [Ref. 18].

For a composite with zero flaws, fatigue is solely matrix controlled with crack initiation taking up a significant portion of the fatigue life. The ability of the matrix material to sustain cyclic loading is dependent on the stress amplitude only; therefore, crack propagation in the matrix can be reduced by controlling the stress amplitude [Ref. 19]. Since it is impossible to manufacture flawless MMCs and since little is understood about MMC fatigue at this time, no generalization about fatigue properties can be made.

There is also a size effect related to three point bend fatigue. Generally, as the cross sectional area increases, by increasing the height, the fatigue life decreases. This is due to an increase in strain at the outer surface, the area of maximum strain when in tension.

Equation 2 shows the relationship between strain, ϵ , and specimen height, h , for three point bending fatigue.

$$\epsilon = \frac{6 \times \delta \times h}{L^2} \quad (2)$$

Figure 3 shows a schematic of a three point bend fatigue apparatus. Bend fatigue investigation is of interest since the mounting frame for an electronic module is a flat plate that is subjected to cyclic bending loads. Because crack initiation already exists, each type of MMC must be tested individually to determine their crack propagation, and fatigue properties.

C. RESEARCH OBJECTIVES AND OVERVIEW

The purpose of this research is two fold. The first objective is to investigate the effects thermal cycling has on diffusion bonded, P100 graphite fiber reinforced 6061 aluminum [0/90] laminate MMCs. This will be done using a thermal cycling apparatus, a dilatometer, replicas made using acetate tape, and microscopy.

The second objective is to investigate the bend fatigue properties of cast, P100 graphite fiber reinforced 6061 aluminum [0/90] laminate MMCs using the MTS 810 test system and microscopy. The composite's bend fatigue properties will be compared to those of the 6061 aluminum monolith.

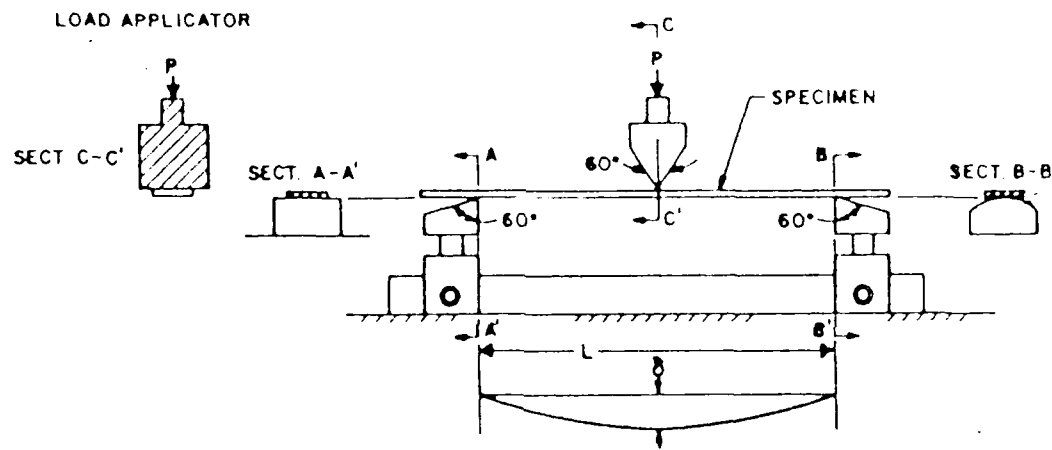


Figure 3: Schematic of a three point bend fatigue apparatus.

III. EXPERIMENTAL EQUIPMENT AND TECHNIQUES

A. THERMAL CYCLING

A schematic of the apparatus used to thermally cycle samples is shown in Figure 4. A Eurotherm temperature controller, model 808, was used to maintain a Marshal tube furnace, model 1134, at a uniform temperature.

Two chromel-alumel, type K, thermocouples were used to measure temperatures. One thermocouple was used by the Eurotherm controller to measure and control the temperature of the furnace and one was used to measure the temperature which the samples were subjected to.

A brass capsule was used as a holder and environmental chamber for the samples. The brass capsule was inserted into and removed from the furnace via a pneumatic piston. A solenoid valve controlled by a Chontrol digital timer was used to direct air to the piston.

Temperature profiles were obtained using a strip chart. Figure 5 shows a typical temperature profile the square samples were subjected to.

Microscopy of the thermally cycled samples was accomplished using edge replicas, scanning electron microscope (SEM), and transmission electron microscope (TEM). The replicas were used to examine macro-damage caused by cycling while the SEM was used to examine micro-damage. Appendix B explains the procedure used to produce the

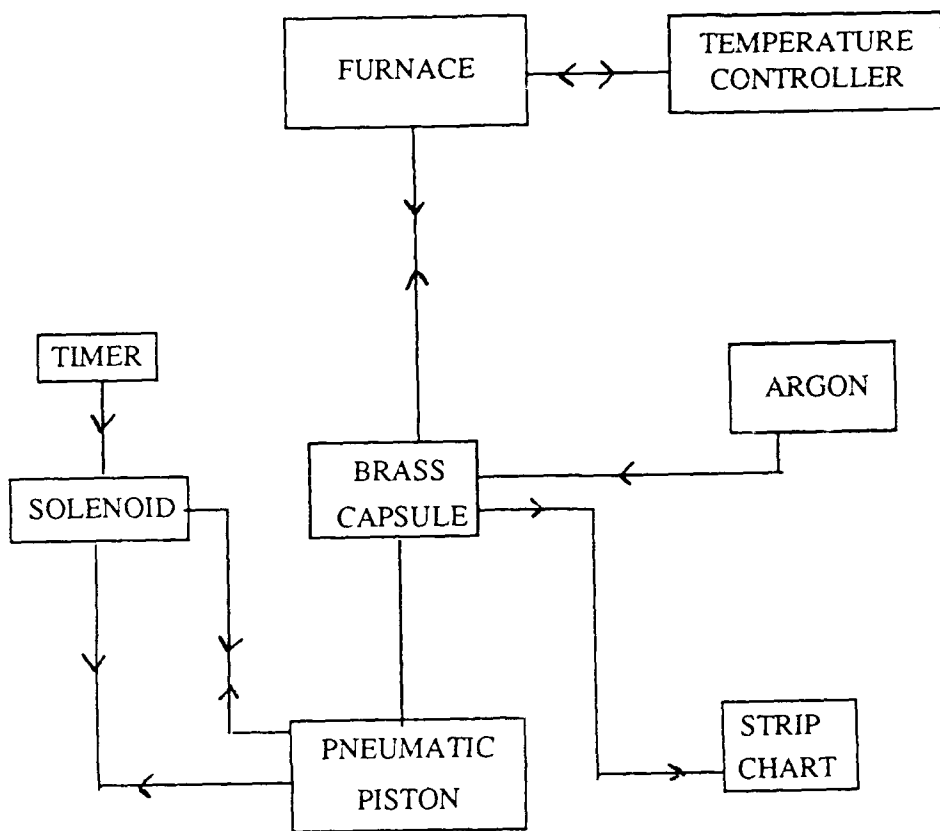


Figure 4: Schematic of the apparatus used to thermally cycle samples.

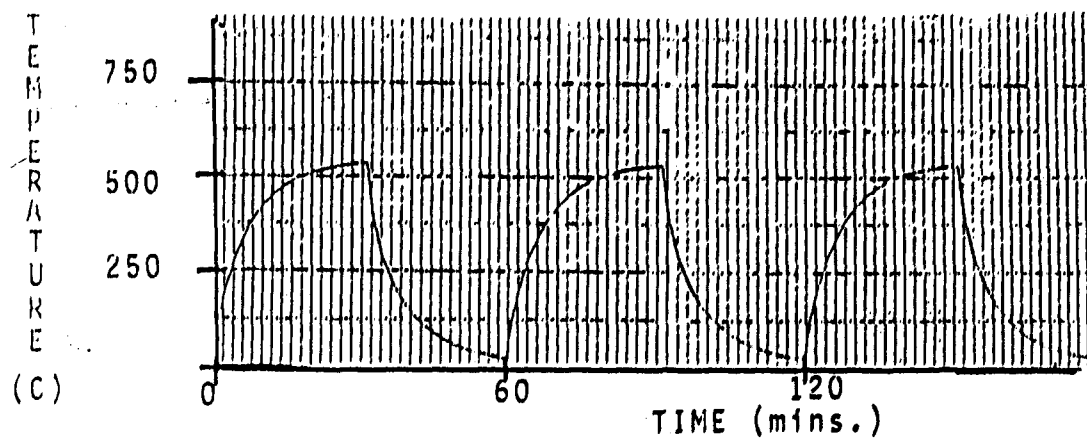


Figure 5: Typical temperature profile samples were subjected to.

replicas. The TEM was used to analyze the micro constituents at the fiber/matrix interface region, and to determine the aging state of the matrix.

An Orton™ dilatometer (0 - 1500 °C range, manufactured by the Edward Orton Jr. Ceramic Foundation of Ohio) was used to measure thermal strain of the Al-Gr composite. Because we were only using approximately 10% of the dilatometer's full range, a Hewlett Packard data acquisition unit, model 3852A, was used to collect data from the dilatometer to facilitate enlarging the plot of percent strain versus temperature. Appendix A explains how the program was used to extract data. Helium or argon was used to create an inert atmosphere in both the capsule and the dilatometer for all runs.

The effect of thermal cycling, up to 100 °C, on the stiffness of the MMC was measured by cycling the MMC up to 500 times in argon and measuring the elastic modulus in bending using a three point bend fixture and an electrohydraulic MTS

machine. The data, presented in the form of elastic modulus in bending versus number of cycles, is indicative of the point at which interfacial debonding between the fiber and matrix occurs (i.e., the fibers no longer stiffen the composite).

Microscopy, percent strain versus temperature diagrams, and the bend modulus versus number of thermal cycles behavior are the basis for evaluation of the MMC subjected to thermal loading.

B. FATIGUE

Three point bend fatigue experiments were conducted using the MTS 810 electrohydraulic test system with the MTS three point bend fixture model 642.05A-01. Sample deflection was measured using an MTS displacement transducer model 632.06B-20, which is specifically designed for the bend fixture used.

All tests were conducted in the load control mode at 10 Hz. The function generator was set to generate an inverted Haver sine so a stress ratio, R, equal to zero could be produced. This means that for one cycle the load would only go from zero, to the maximum set load, then back to zero.

The elastic modulus in bending, E_b , yield stress, σ_y , and the ultimate bending stress (UBS) were determined by producing load versus displacement curves for each type of sample using the three-point bend fixture, the inverted ramping function set to ramp from 0 to 100 lb, in 500 seconds, the displacement transducer, and an X-Y plotter.

The equation for bending stress, equation 3, was determined from solid mechanics to be as follows for three point bending.

$$\sigma = \frac{Mc}{I} = \frac{3 \times P \times L}{2 \times b \times h^2} \quad (3)$$

where P = load, L = span between rollers on bend fixture, b = sample width, and h = sample height. Strain measurement for three point bending is shown in Equation 2.

The equation for E_b for three point bending is

$$E_b = \frac{\sigma}{\epsilon} = \frac{P \times L^3}{4 \times b \times h^3 \times \delta} \quad (4)$$

Displacement data for all samples that were loaded at 90% of their UBS was taken approximately every 1000 cycles, to determine the relevant secant modulus, E_s , response in bending. The equation for E_s is

$$E_{s_i} = \frac{\sigma_{max}}{\epsilon_i} \quad (5)$$

where σ_{max} is based on the maximum load for the run, which was constant, and ϵ_i = strain based on the maximum displacement during the i^{th} cycle. This may or may not exceed the yield strength. If it does and plastic deformation occurs, it does so only in the initial cycle.

Microscopy of the fatigue samples consisted of using the SEM to inspect microscopic damage of the failed region. The optical microscope was used to examine the crack

profiles and the TEM was used to examine the fiber/matrix interface region. All fatigue tests were conducted at room temperature in atmospheric air.

Microscopy, S-N curves, load versus displacement curves, and secant modulus calculations were the parameters used to evaluate the MMC subjected to three point bend fatigue.

IV. EXPERIMENTAL PROCEDURES

A. MATERIALS

1. Thermal Cycling

Thermal cycling was performed on a diffusion bonded, P100 graphite fiber, 45 volume percent, 6061 aluminum laminate with [0/90] cross plies manufactured by DWA Composite Specialties, Inc.. It consisted of 11 plies of variable thickness with a total thickness of 1.65 mm. This composite was used because high quality replicas were easily obtained from it.

The composite used in this study for thermal strain measurement was a P100 graphite fiber, 40 volume percent, 6061 aluminum laminate with [0/90] cross plies also manufactured by DWA Composite Specialties, Inc. using a diffusion bonding process. It consisted of 7 plies of variable thickness with a total thickness of 2.2 mm and had an anodized finish for corrosion protection. The matrix in both composites was overaged, as verified by TEM inspection.

2. Fatigue

The composite used for the fatigue experiments was a cast, P100 graphite fiber, 40 volume percent, 6061 aluminum laminate with [0/90] cross plies manufactured by Fiber Materials, Inc.. It consisted of three graphite layers with a total average thickness of 2 mm. The matrix metal was in an overaged state as verified by TEM inspection.

When discussing fiber orientation related to bend fatigue tests, "longitudinal" will refer to the fibers running parallel to the long axis of the specimen and "transverse" will refer to the fibers running parallel to the short axis of the specimen. The long axis of the specimen will be used as the reference for measuring ply angle. Two fiber orientations are studied; orientation "A", referred to as composite A, has its center fiber layer running longitudinally and orientation "B", referred to as composite B, has its two outside fiber layers running longitudinally. Figure 6 shows a schematic of the fiber orientation convention.

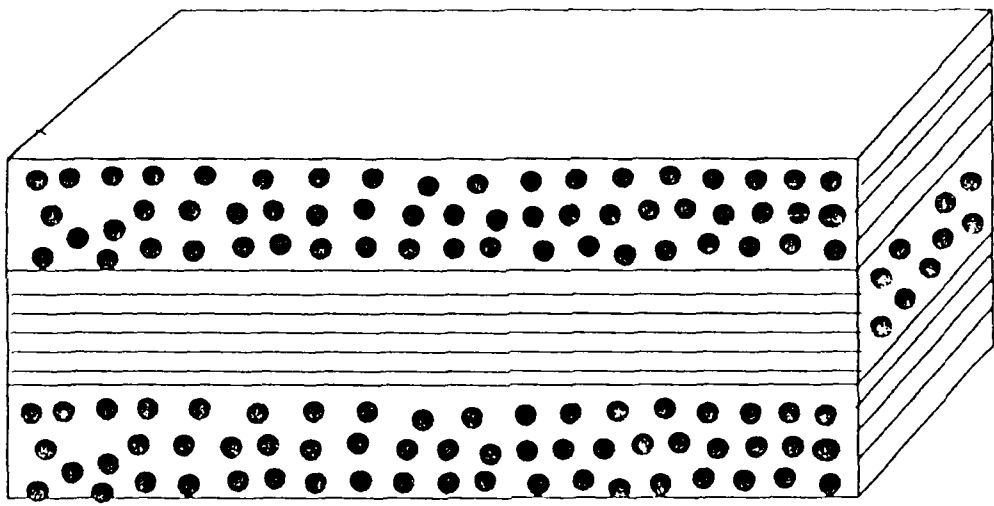
A 6061-T6 aluminum alloy monolith, manufactured by ALCOA, was heated to overage it and was used as a reference for comparing the properties of the MMC.

B. PROCEDURES

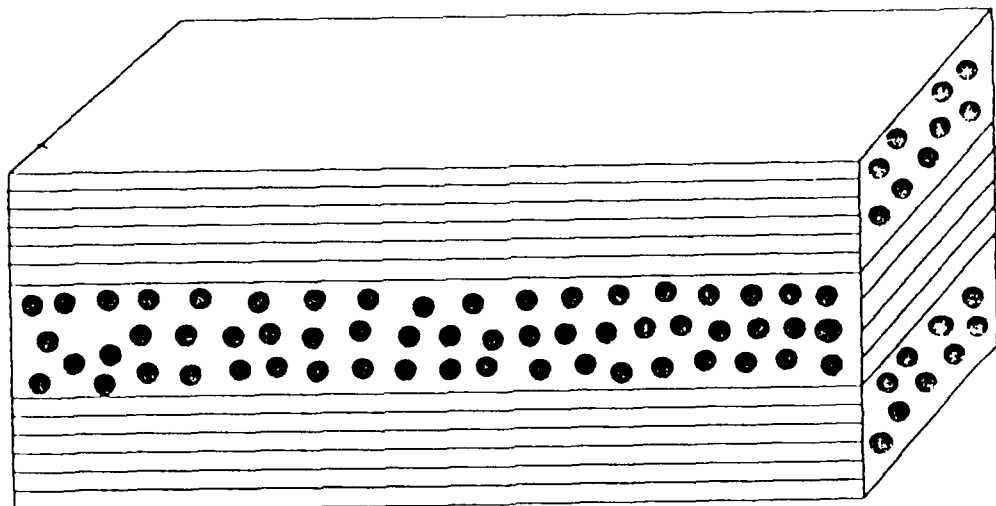
1. Thermal Cycling

The composite used for thermal cycling experiments was cut into square samples approximately 7 mm by 7 mm. The shape was more important than the size to insure thermal expansion was equal in all directions. The edges were then wet sanded using 240, 320, 400 and 600 grit paper respectively and polished using 1 μm diamond paste to eliminate as many edge defects as possible. One edge was marked to ensure all replicas for that sample were taken from the same edge. A replica was made of the marked edge of each sample prior to thermal cycling.

The samples were then sealed in the brass capsule (in an argon atmosphere) and thermally cycled in the tube furnace on a 30 minute heating cycle, with 10 minutes at the temperature of interest, see figure 5. The furnace was preset at either 540 °C or 100 °C.



(a)



(b)

Figure 6: Schematic of the fiber orientation convention: (a) composite A, center fiber layer runs longitudinally, (b) composite B, the two outside fiber layers run longitudinally.

Replicas were taken periodically during the cycling process. The frequency at which replicas were taken depended on the maximum temperature of cycling. Optical examination of the replicas, SEM observations of the as-cycled sample edges, and TEM inspection of the fiber/matrix interface of one sample that was cycled at the high temperature (540 °C) was undertaken.

For dilatometry experiments, samples were cut rectangular in shape measuring approximately 26 mm by 6 mm. The ends were rounded slightly to ensure only one point of contact at each end. The longitudinal edges were wet sanded using 240, 320, 400 and 600 grit paper respectively and polished using 1 µm diamond paste. The final length of each coupon was 25.4 mm (1 inch); since the Orton™ dilatometer is calibrated for one inch samples only. All samples were cut so the laminate layers in each sample had the same orientation. Figure 7 is a schematic of the samples used for strain measurements in the dilatometer.

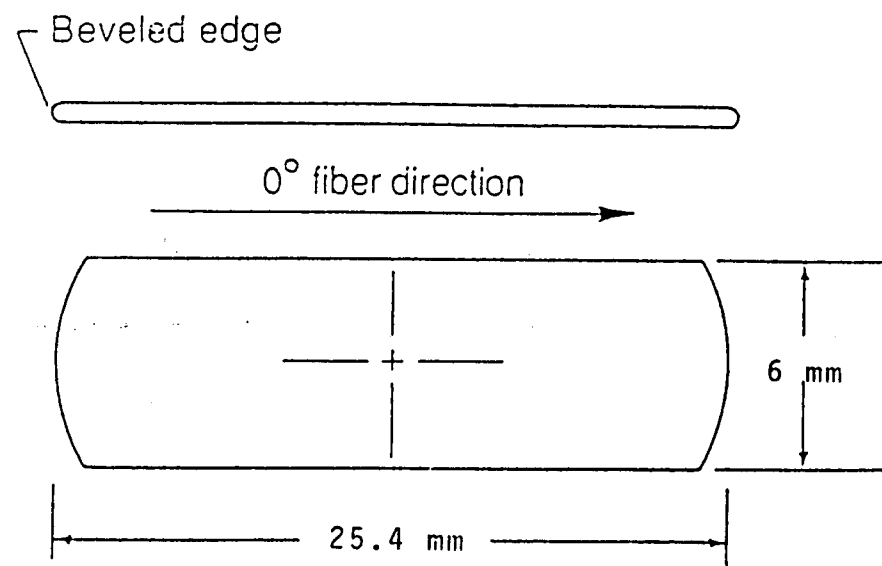


Figure 7: Schematic of samples used for dilatometry experiments.

The dilatometer was first used to measure thermal strains in a 25.4 mm bar of high purity alumina as a calibration step. No hysteresis was observed for heating and cooling rates of 0.89 °C/min. and 0.31 °C/min., respectively, between room temperature and 540 °C. These heating and cooling rates were then used with the composite samples ensuring any observed hysteresis as real sample effects. Cycling was done in an argon atmosphere between room temperature and i) 100 °C, ii) 540 °C.

The data obtained from the dilatometer was in the form of millivolts which was reduced using the Hewlett Packard data acquisition unit and a computer program (appendix A). The reduced data was then entered into a MacIntosh computer to facilitate enlarging the plots of percent strain versus temperature for various cycles.

Finally, the effect of thermal cycling up to 100 °C on the stiffness was evaluated as stated in section III. A.

2. Fatigue

The samples, both composite orientations and the monolith, were cut to the nominal size of 50 mm by 4.5 mm. The edges were then wet sanded using 240, 320, 400 and 600 grit paper respectively and polished using 1 µm diamond paste to eliminate as many crack initiation sites as possible. The final width was approximately 4 mm. The sample dimensions were restricted due to the bend fixture design. The maximum width was 4 mm with a minimum length of 45 mm to ensure the samples remained on the rollers for the entire run. The cross sectional dimensions of each sample were carefully measured after polishing.

Prior to sanding and polishing, the monolith samples were heat treated at 200 °C for four hours to cause overaging and thus matching the matrix state in the composite.

Load versus displacement curves were produced first, as explained earlier, to determine the yield stress, the elastic modulus in bending, the UBS, and the proof strength, S_p , of composite A, composite B and the monolith. Proof strength is the point at which plastic deformation occurs, and is determined by using a 0.01% strain offset.

The samples were then cycled at various stress levels based on their respective UBS (i.e., maximum stress = $S_{max} = (x\%)(UBS)$). The stress ratio for all runs was $R = 0$. Number of cycles to failure and S_{max} were recorded for all samples. The secant modulus was also record, as mentioned earlier, for samples cycled at 90% of UBS.

Composites A and B cycled at 90% UBS where mounted in epoxy after failure and polished using 0.05 μm Alumina to examine the crack profiles of both orientations using a light microscope.

V. RESULTS AND DISCUSSION

A. THERMAL CYCLING

Figure 8 shows the edge replica of the diffusion bonded composite prior to cycling. Owing to the large fiber volume the liquid infiltration was imperfect leading to fiber clustering and poor wetting; consequently, some voids can be seen in figure 8. Figure 9 shows the edge replica of the diffusion bonded composite, cycled up to 540 °C for 3 hours (3 cycles) in an argon atmosphere. Cracks can be seen to have originated in the transverse fiber layer and moved along paths of easy propagation formed by the existing voids. Inspection of the adjacent edges also showed similar cracking. Since the residual stresses for thermal cycling up to 540 °C can fluctuate between large tensile and compressive values, even a few cycles can give rise to large damage accumulation as seen in figure 9. Evidence of these large tensile and compressive thermal residual stresses generated at the extremities of thermal cycles between 25 °C and 540 °C is obtained from the subsequent dilatometry experiments.

Besides these large cracks, another form of damage due to cycling is fiber/matrix debonding. Both types of damage can be seen in figures 10 and 11, which show SEM micrographs of a large crack and fiber protrusion from the composite surface, respectively. The sample was cycled for 72 hours (72 cycles) up to 540 °C in argon. Fiber protrusion occurs because the fibers were under axial compression in the fully consolidated composite at room temperature. Subsequent cycling and poor interfaces, as



Figure 8: Edge replica of the uncycled MMC showing both 0 and 90 degree laminates. The arrow indicates a void. Magnification = 200X.

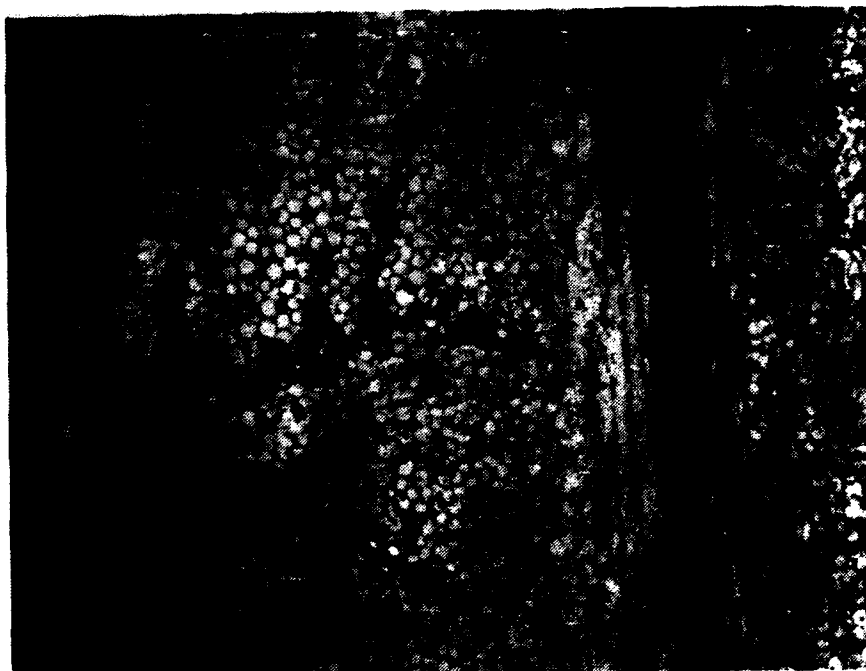


Figure 9: Edge replica of the same MMC after 3 cycles in Argon at 540 °C. Cracks are seen to have originated in the transverse layers. Magnification = 200X.



Figure 10: SEM micrograph showing a large crack propagating through a transverse fiber layer after 72 thermal cycles.

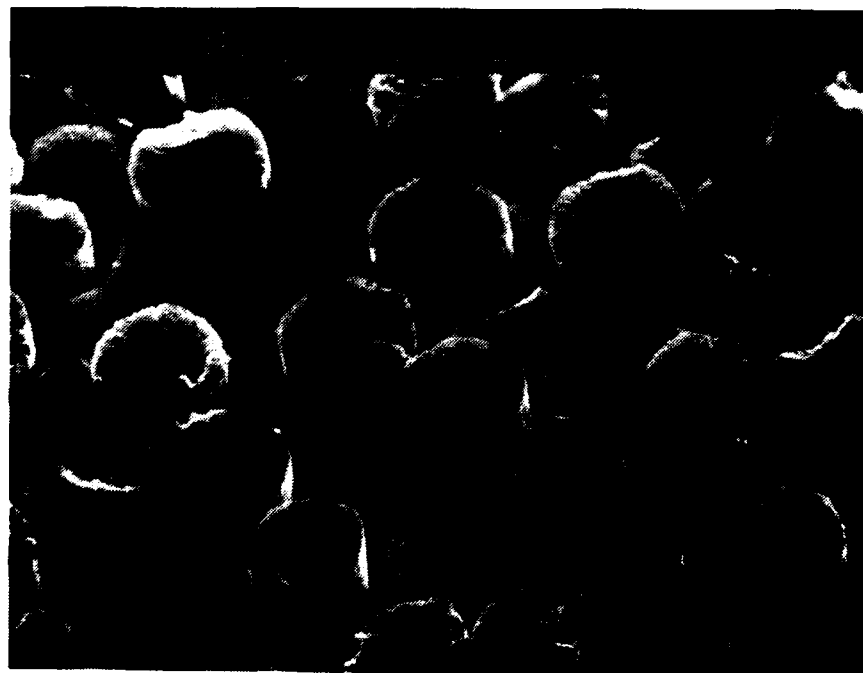


Figure 11: SEM micrograph of the MMC showing protruding fiber ends, indicating interfacial debonding.

seen by TEM observations (reported later), ensure debonding and fiber expansion leading to some fiber protrusion.

As discussed in section II.A.1, unidirectional Al-Gr composites have resident tensile residual stresses along both the longitudinal and transverse directions. Therefore, the in-plane residual stresses in a cross plied Al-Gr composite laminate are expected to be tensile along both the longitudinal and transverse directions. The through thickness stresses are comparatively small since the laminate thickness is small, and hence, can be ignored. This residual stress-state in the composite is responsible for the thermal excursion behavior of the composite, as will be elucidated in the subsequent discussion.

Figure 12 plots the thermal percent strain between 25 °C and 540 °C for up to 10 cycles. A large residual strain (A-E) is seen after the first cycle indicating overall tensile yielding. During the initial segment A-B, the extremely large initial tensile residual stress in the matrix is relieved. Two effects now occur during heating; the yield strength of the matrix keeps reducing and the induced tensile residual stresses start getting relieved. If the yield strength reduces faster than the tensile residual stresses, plastic yielding can occur. Additionally, visco-plastic deformation can also occur due to the slow heating rate. This process is similar to creep elongation at moderate, homologous temperatures and does not lead to any significant strengthening of the matrix. Also, the tensile residual stress aids the expansion of the matrix and results in the large CTE for segment A-B. Complete unloading occurs at around 200 °C at which point the thermal expansion behavior is that of a composite without any residual stresses (i.e., governed by : retical rule of mixtures type of calculations). Further heating, segment B-C, introduces

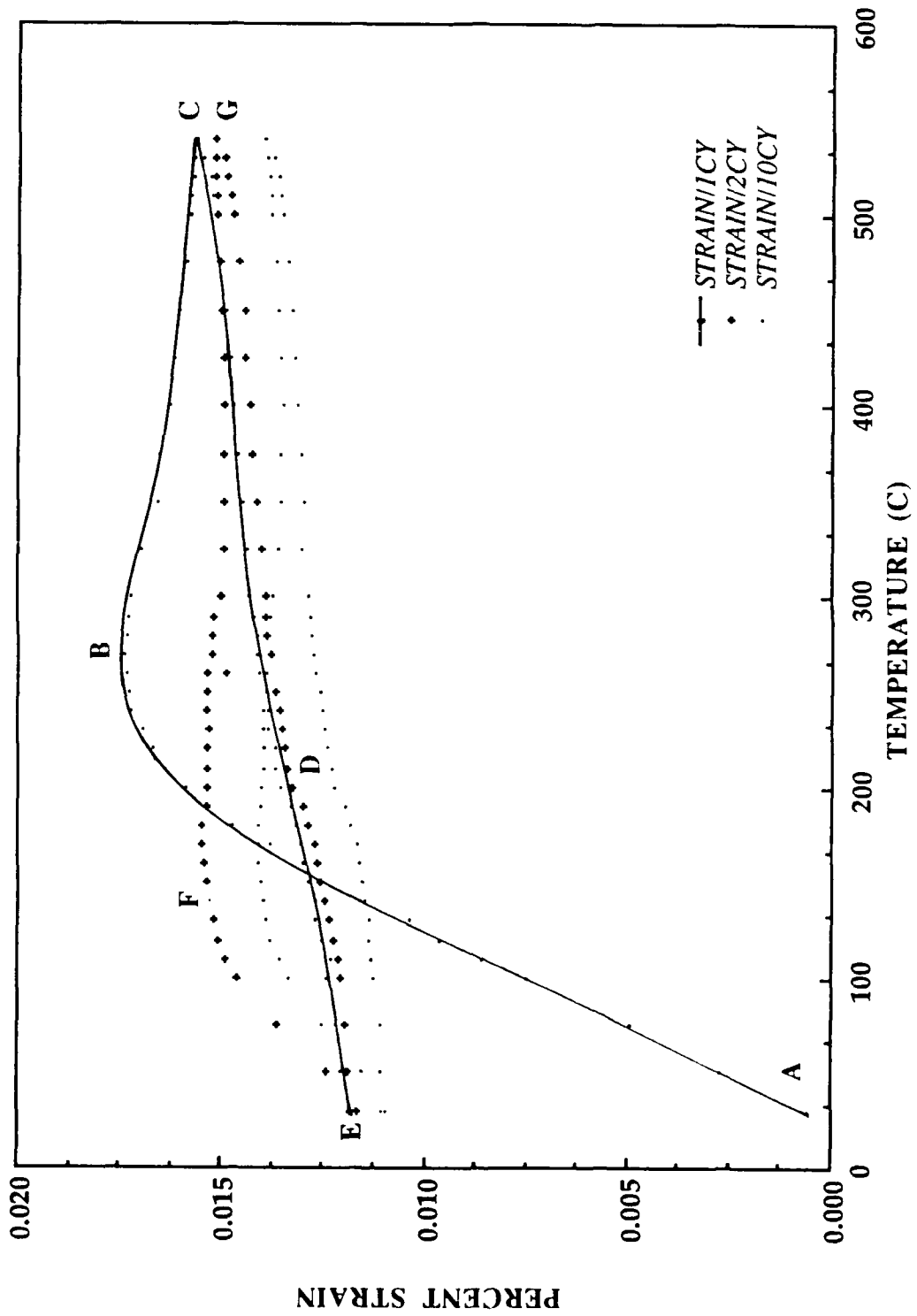


Figure 12: Thermal percent strain versus temperature for the range of 25C to 540C, upto 10 cycles.

compressive residual stresses which oppose any further expansion. Once again, yielding can occur if the compressive stresses exceed the constantly reducing yield strength. The compressive stress state at C gets relieved on cooling in segment C-D. The residual compressive stress however assists the contraction due to cooling, resulting in the hysteresis between segments B-C and C-D. The segment D-E has tensile residual stresses build up again, but to much smaller values as compared to the tensile residual stress before the first cycle. Also, the tensile residual stress opposes contraction of the composite, which is necessary to retrace its initial A-B segment. Consequently, tensile residual strain exists. Subsequent cycling then starts with a much smaller tensile residual stress. Figure 12 shows stress relieving at lower temperatures during the second cycle and has little tensile elongation in the initial slope E-F (much shallower slope than that of segment A-B). There exists a slight compressive strain after the second cycle which can be explained as follows.

The compressive residual stress set up in segment F-G, is large and can cause yielding in addition to creep deformation. On cooling, from G, the compressive residual stress once again aides contraction. The observed hysteresis arises from the opposition to expansion by the compressive stresses in segment B-C, followed by the enhancement of contraction by the compressive stress in segment C-D. The large residual plastic strain after the first cycle (segment A-E) can be attributed largely to tensile yielding of the matrix due to the large initial tensile residual stress. In addition, some visco-plastic relaxation (creep) occurs throughout the thermal excursion, leading to further plastic deformation. The sharp decrease in the residual plastic strain in successive cycles is

attributed to the substantially reduced tensile stress present at the end of the first cycle.

Hysteresis still exists, with very little change after 10 cycles.

This behavior differs significantly from that of a unidirectional ply Al-Gr composite as measured by Dries and Tompkins [Ref. 20]. In the room temperature to 250 °F segment, these authors found a net compressive residual strain even for the first cycle. This was attributed to relatively small initial tensile residual stresses at room temperature. Also, the hysteresis reduced sharply with cycling [Ref. 20]. This is clearly not the case here and is explained by inspecting the cause for the hysteresis in the first place. Dries and Tompkins [Ref. 20] attributed it to plastic yielding of the matrix with relatively fast heating and cooling rates. In the experiments performed in this work, the hysteresis is attributed to the presence of residual stresses preventing reproducible thermal strains.

Figure 13 plots thermal percent strain up to 100 °C. Once again the residual stress state is seen to play a role. The cooling segment B-C is at higher strain levels than the heating segments. This is because the large tensile residual stress is being incompletely relieved at 100 °C and opposes the contraction behavior (the average CTE for segment A-B is greater than the average CTE for segment B-C). Once again, hysteresis exists since the tensile residual stress opposes reproducible strain behavior in segment B-C. The large tensile residual stress at A is partially relieved due to the creep deformation leaving a smaller tensile residual stress at C that is insufficient to cause any further plastic deformation but does play a role in hysteresis effects.

In addition to hysteresis and the generation of residual plastic strains, thermal cycling results in degradation of the interface and debonding due to poor interfaces. This

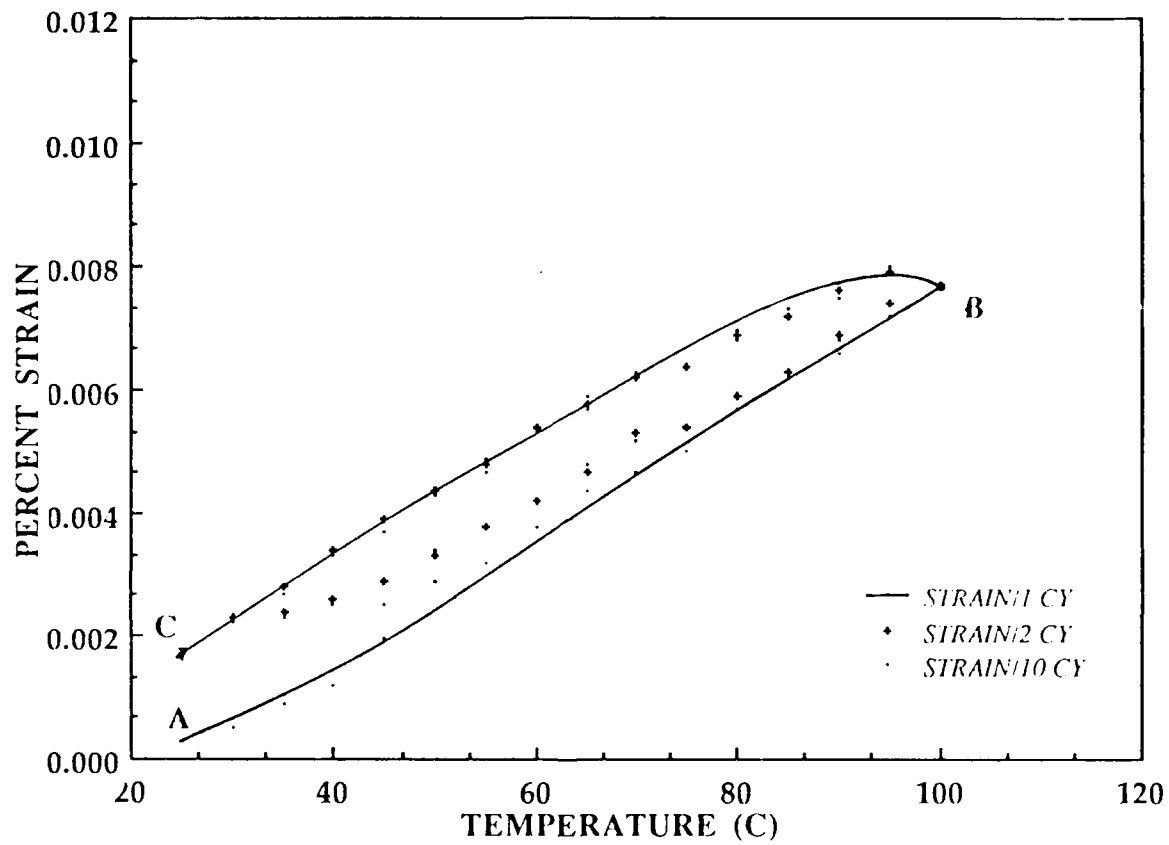


Figure 13: Thermal percent strain versus temperature up to 100 °C for unprocessed sample up to 10 cycles.

degradation can be evaluated by measuring the elastic modulus as a function of thermal cycling. This data is plotted in Figure 14, which shows elastic modulus in a three point bend test versus number of cycles at 100 °C in argon. Also plotted is the bending proof strength (0.01% offset). The modulus curve shows serious degradation from around 100 cycles onwards (indicated by a drop in modulus value), and is attributed to fiber/matrix debonding (i.e., the fibers no longer stiffen the matrix).

To study the effects of residual stress, a thermal treatment was given to the samples, viz., aging at 200 °C for four hours followed by quenching to room temperature or liquid nitrogen temperature. The 200 °C to room temperature sample should have had most of its tensile residual stresses annealed out at 200 °C (see figure 12). Thus quenching to room temperature would result in a small tensile residual stress due to the small ΔT (see equation 1). When this sample is now cycled between room temperature and 100 °C the residual strain observed after the first cycle is negligible since the initial tensile residual stress is small, although hysteresis is still evident (see figure 15). Furthermore, the average CTE for the heating segment of the first cycle is lowest for this sample signifying a very small tensile residual stress at room temperature.

Figure 16 shows the liquid nitrogen quenched sample with a ΔT of approximately 400 °C, which exhibits a large residual strain after the first cycle. This is due to the added tensile residual stresses introduced during the quench. Compared with figure 15, this is larger owing to the larger tensile residual stress before the first cycle. Consequently, the average CTE during the heating segment of the first cycle is also larger ($1.1 \times 10^{-6}/\text{°C}$ as compared to $1 \times 10^{-6}/\text{°C}$ for the sample quenched to room temperature). Due to stress

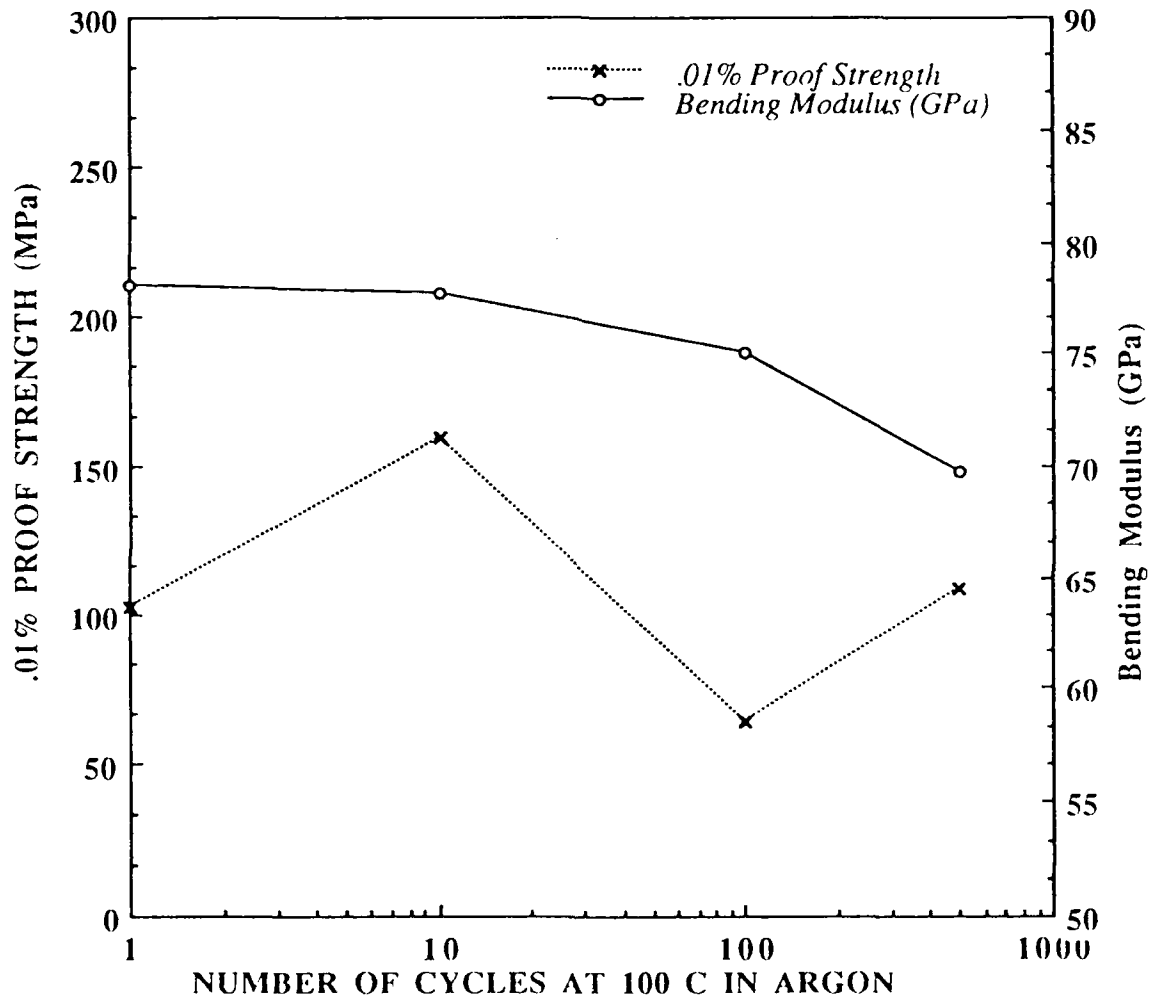


Figure 14: Plot of the elastic modulus in bending and 0.01% proof strength versus the number of thermal cycles at 100 °C.

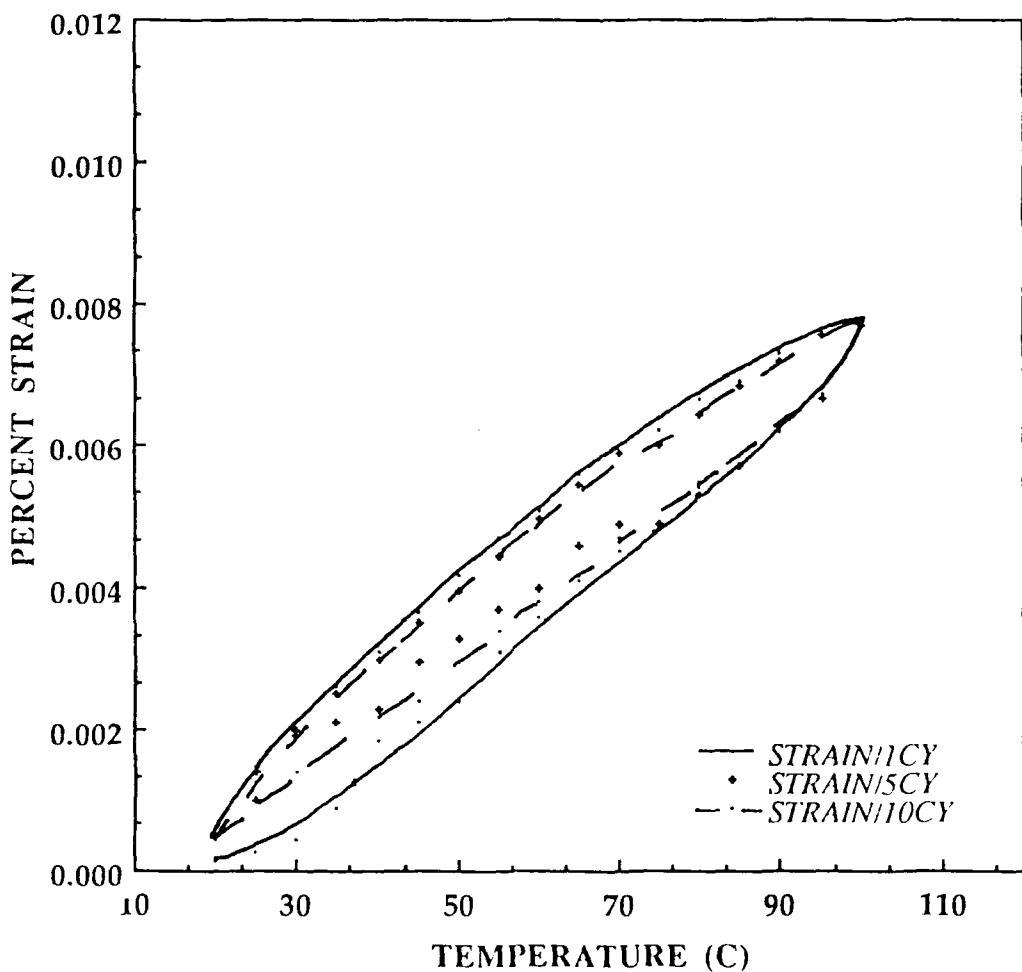


Figure 15: Thermal percent strain versus temperature, up to 100 °C, for sample heated to 200 °C and water quenched to room temperature.

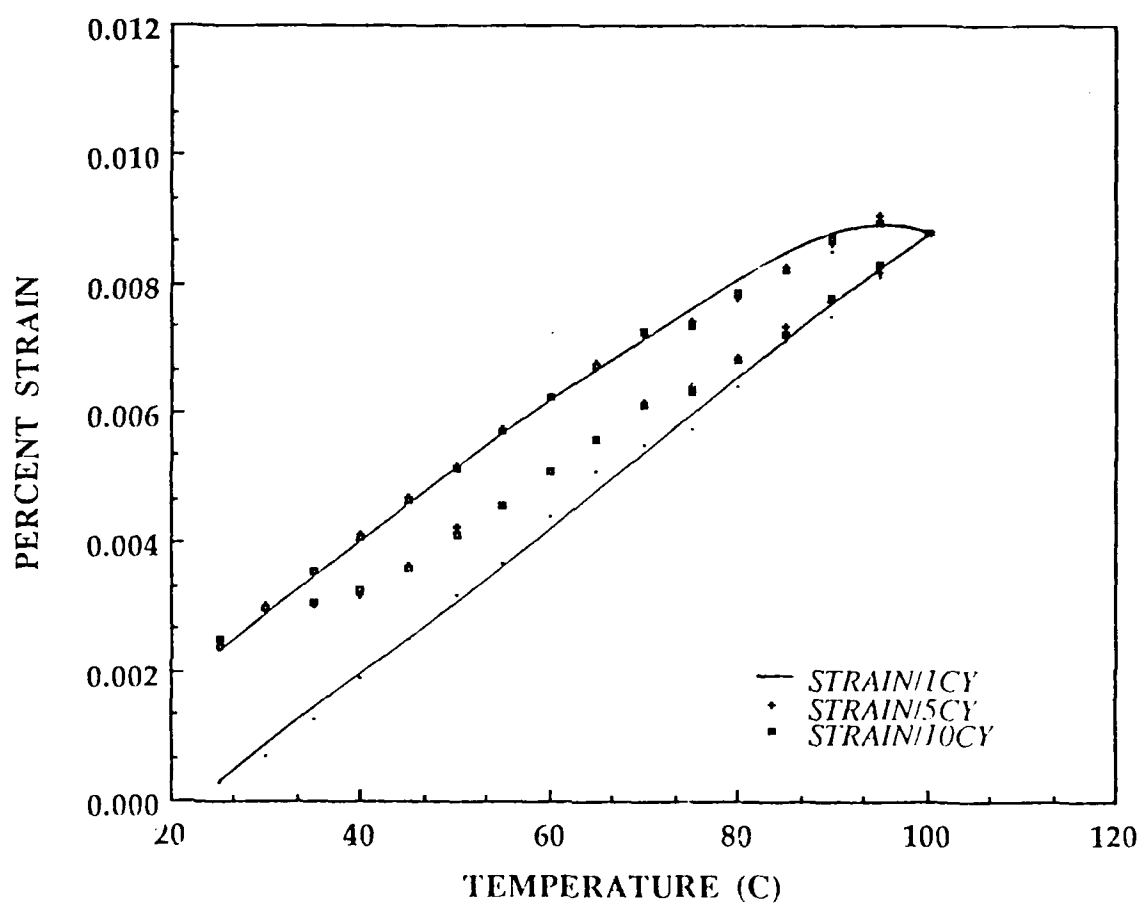


Figure 16: Thermal percent strain versus temperature, up to 100 °C, for the sample heated to 200 °C and quenched in liquid nitrogen.

relief (via creep relaxation) after the first cycle, the average CTE values of figure 15 and 16 are approximately equal from the second cycle onward.

Finally, the transmission electron micrographs, shown in figure 17, examine a typical interface between the fiber and the matrix. A TiB_2 layer is usually applied on the fibers by CVD of Ti and B before liquid metal infiltration. As seen from figure 17, the matrix side of the interface has a fine distribution of particles. The corresponding diffraction pattern (inset figure 18) shows these particles to be TiB rather than TiB_2 . This is checked by comparing "d" spacings from the ring pattern with published "d" spacings for both TiB and TiB_2 . Figure 18 is a centered dark field image using the region of the ring shown and lighting up some of the TiB particles present. Evidently, the desired coating did not form and the TiB was dislodged during the liquid metal infiltration process. The interface in a sample cycled up to 540 °C for 72 hours (72 cycles) showed no additional features. No evidence of any carbide formation was observed, probably because the total time at temperatures above 500 °C was about 12 hours, insufficient for the formation of Al_4C_3 . Thus chemical degradation of the interface is not a factor in these high temperature cycling experiments and all results can then be explained with mechanical effects.



Figure 17: Bright field TEM micrograph showing fine particles on the matrix side of the interface. These particles are concentrated approximately $0.5 \mu\text{m}$ from the interface. Magnification = 40,000X



Figure 18: TEM centered dark field of the same region as figure 17, with the objective aperture centered around the point labeled X, lighting up the TiB particles. Magnification = 40,000X.

In conclusion, from the thermal cycling experiments, the following points can be made:

- Two types of defects are introduced during cycling,
 - (a) large cracks due to thermal residual stresses (high temperature amplitude cycling).
 - (b) fiber/matrix debonding (high and low temperature amplitude cycling).
- The thermal strain behavior of a cross plied composite depends strongly on the residual stress state of the matrix before cycling begins.
- Thermal strain hysteresis exists at slow heating and cooling rates, even for cycling at low temperatures, due to residual stresses aiding or opposing the expansion or contraction behavior of a [0/90] Al-Gr MMC.
- Creep deformation effects exist at slow heating and cooling rates and has to be included in any strain analysis of composites in thermal cycling conditions.
- Permanent strain, attributed to the presence of large tensile residual stresses initially, exists after the first cycle and depends on the magnitude of the residual stress present before cycling begins. Heat treatment (at 200 °C) for the [0/90] cross ply Al-Gr MMC can relieve the residual stress to the extent that no permanent strain exists after the first cycle of subsequent thermal cycling.
- Cumulative damage due to fiber debonding on cycling up to 100 °C is attributed to poor interfacial strength associated with the lack of a continuous, adherent TiB₂ layer on the graphite fiber.

B. FATIGUE

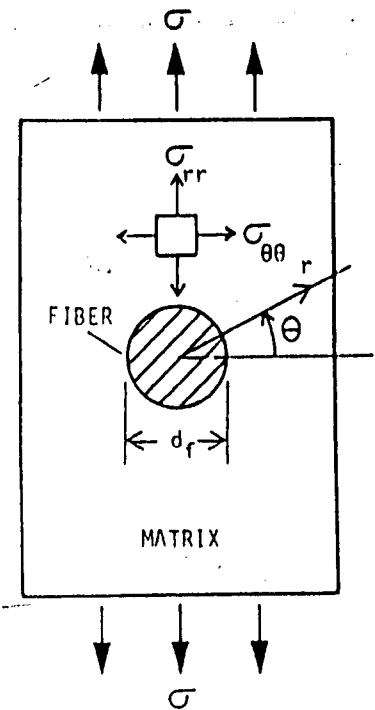
Table 1 shows the properties of the samples based on their respective load versus displacement curves.

TABLE 1: Properties of the test specimen.

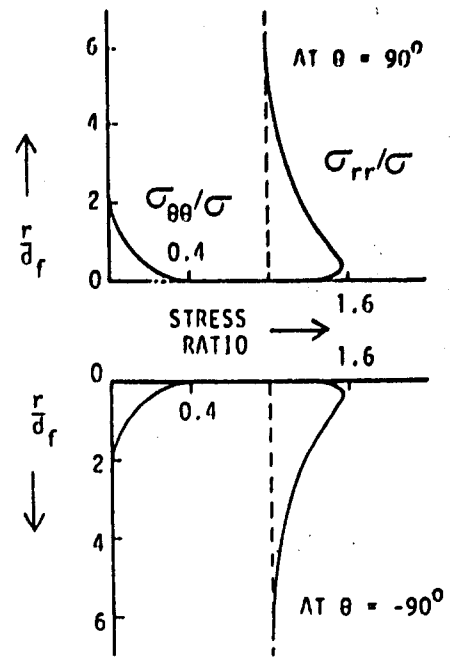
	E_b (GPa)	UBS (MPa)	S_p (MPa)	Maximum Deflection (mm)
Composite A	47.6	205.94	132.3	0.8077
Composite B	221.0	388.0	367.0	0.274
Monolith	70.9	444.3	316.5	2.134

The table shows the monolith having a higher bending stiffness than composite A, which was unexpected. Also unexpected was the monolith having a higher UBS than either composite. Although these results were unexpected, they are the actual responses of the materials and are due to the manufacturing flaws present in the composite. Also, stress concentration due to the fibers, along with inherently weak interfaces, could be a factor here.

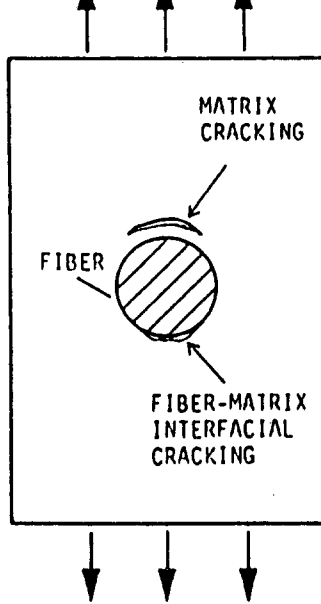
Figure 19 shows a schematic of the radial stress associated with the fibers when loaded in a transverse manner. This radial stress is tensile and approximately 50% greater than the applied stress. In a high fiber volume lamina, there will be stress field interactions from neighboring fibers, increasing the concentrated stress. Because of the radial stress and its interaction with neighboring stress fields, cracks may develop normal



(a)



(b)



(c)

Figure 19: (a) Transverse tensile loading on a lamina with one cylindrical fiber, (b) the stress distribution around the single fiber due to transverse tensile loading, (c) possible micro-failure modes. [Ref. 21]

to the load at the fiber/matrix interface or in the matrix, since stress concentration maxima occur in the matrix, slightly away from the interface. [Ref. 21]

Composite A is more affected by the radial stress effect than composite B. The transverse fibers of composite A are further from the neutral axis than composite B's transverse fibers, leading to larger stress concentration levels. The matrix in composite A may be unable to support the large radial stresses leading to matrix cracking, or interfacial debonding; in either case, composite A will appear to be the weaker configuration due to the larger concentrated, transverse stresses involved. The existence of numerous flaws in the as-fabricated composite, and the relatively poor interfaces, are responsible for dropping the UBS of both composite sample configurations below that of the monolith. The trend in the bending modulus values can be explained as being caused by poor wetting during infiltration and thus incomplete consolidation of the composite, so that the use of the outer dimensions for a single, coherent cross sectional area supporting the load, is not accurate. Consequently, these internal voids will reduce the load bearing cross sectional area and lead to lower values of bending modulus (and strength). Both composite A and B have had their modulus values decreased, but A being the lower value to begin with, falls below the E_b of the monolith.

These flaws have been accounted for in subsequent experiments by normalizing the maximum applied stress with the UBS for the particular specimen being tested.

The secant modulus for composites A, B, and the monolith at 90% UBS is shown in figure 20. Table 2 shows that the stress level, at which the secant modulus was calculated, was in the elastic region of composite B and in the plastic region for composite A and

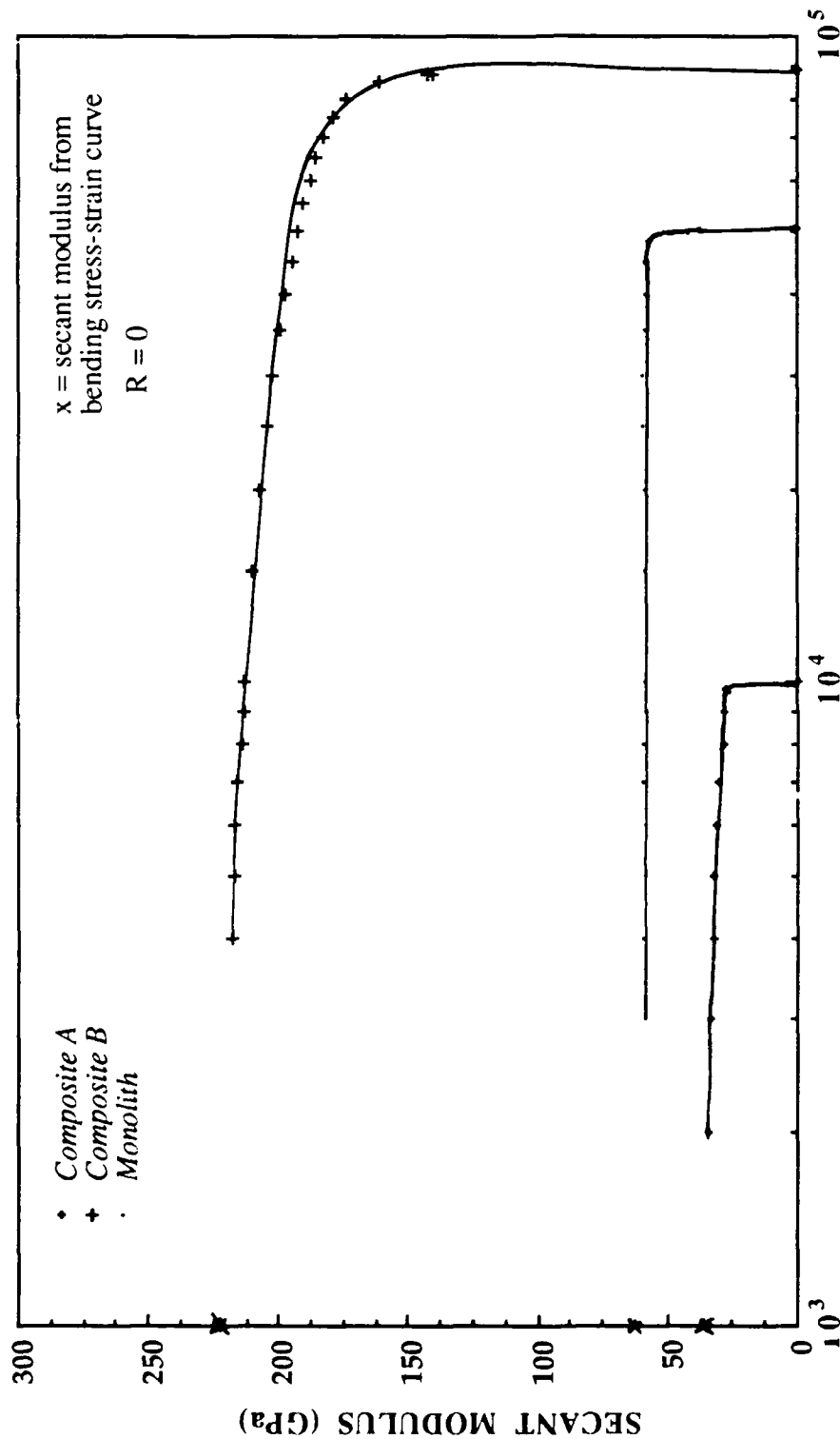


Figure 20: Plot of secant modulus versus number of cycles for all three specimens.

the monolith. The initial drop in E_s for composite B is very small due to the stress level being in the elastic range. The slowly, sloping curve that follows the initial drop is indicative of crack propagation and indicates fatigue failure in composite B is crack propagation controlled with slow accumulation of damage. Since crack initiation occurs early in the fatigue life of composites due to flaws caused by manufacturing, this trend was expected.

TABLE 2: Data used to produce S-N curves.

	S_{max} / UBS	S_{max} (MPa)	S_p (MPa)
Composite A	0.8	164.7	132.3
	0.86	175.0	
	0.896	181.2	
	0.9	184.8	
	0.95	195.6	
Composite B	0.8	310.4	367.0
	0.87	337.6	
	0.903	349.2	
	0.95	368.6	
Monolith	0.65	288.8	316.5
	0.7	310.99	
	0.81	355.4	
	0.9	399.9	

The initial drop in E_s was much greater for composite A and the monolith due to being cycled in the plastic region. The flat curve following the initial drop of the monolith curve is indicative of no crack propagation which means the monolith's fatigue failure is crack initiation controlled. Crack initiation in the monolith occurs at approximately 46,000

cycles, and failure occurred shortly after at 49,750 cycles. This indicates that once damage occurs, damage accumulation is very rapid.

Composite A showed a very slowly sloping curve after the initial drop that increased slightly near the end. Since crack initiation in composites occurs early due to flaws, this behavior can be associated with slow crack propagation rate initially, followed by a rapid crack growth rate after approximately 3000 cycles until failure, a 2 stage propagation.

Figure 21 shows the normalized S-N curves for all three specimens. The curves show an endurance limit for both composites A and B, but not for the monolith. The monolith curve clearly shows the strain controlled and stress controlled regions; the transition point coincides closely with the S_p of the monolith. The endurance limit for composite A coincided with its S_p .

Figure 22 shows the S-N curves using the actual stress levels. Composite A is shown to be the worst for bend fatigue applications. This is due to the radial stress effect on the transverse fibers. Composite B shows to be the best lay-up for high cycle fatigue only; again, the radial stress effect and initial flaws causes the composite to be weaker than the monolith in low cycles fatigue situations.

Optical micrographs of composite A are shown in figures 23 and 24. Figure 23 shows a macroscopic view of the crack. Crack initiation was observed inside the tensile loaded transverse layer and was seen to propagate outward (towards the surface) and inward into the next layer. Crack propagation in the longitudinal layer then took the form of fiber breaking, evidenced by a substantial lack of fiber/matrix debonding, as seen in figures 23 and 24. Figure 24 also shows fiber buckling in the compressive region.

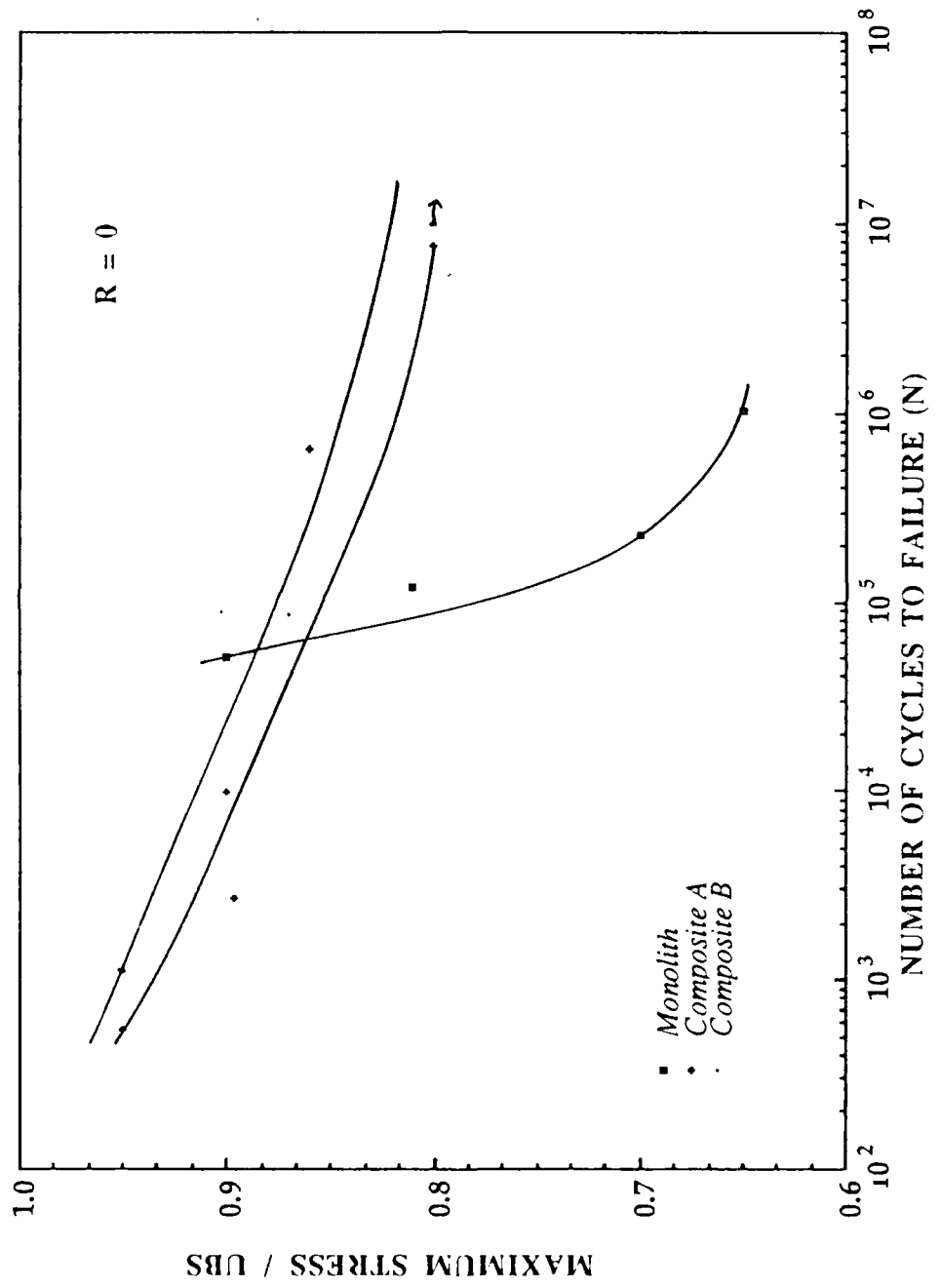


Figure 21: Normalized S-N curves for all three specimens.

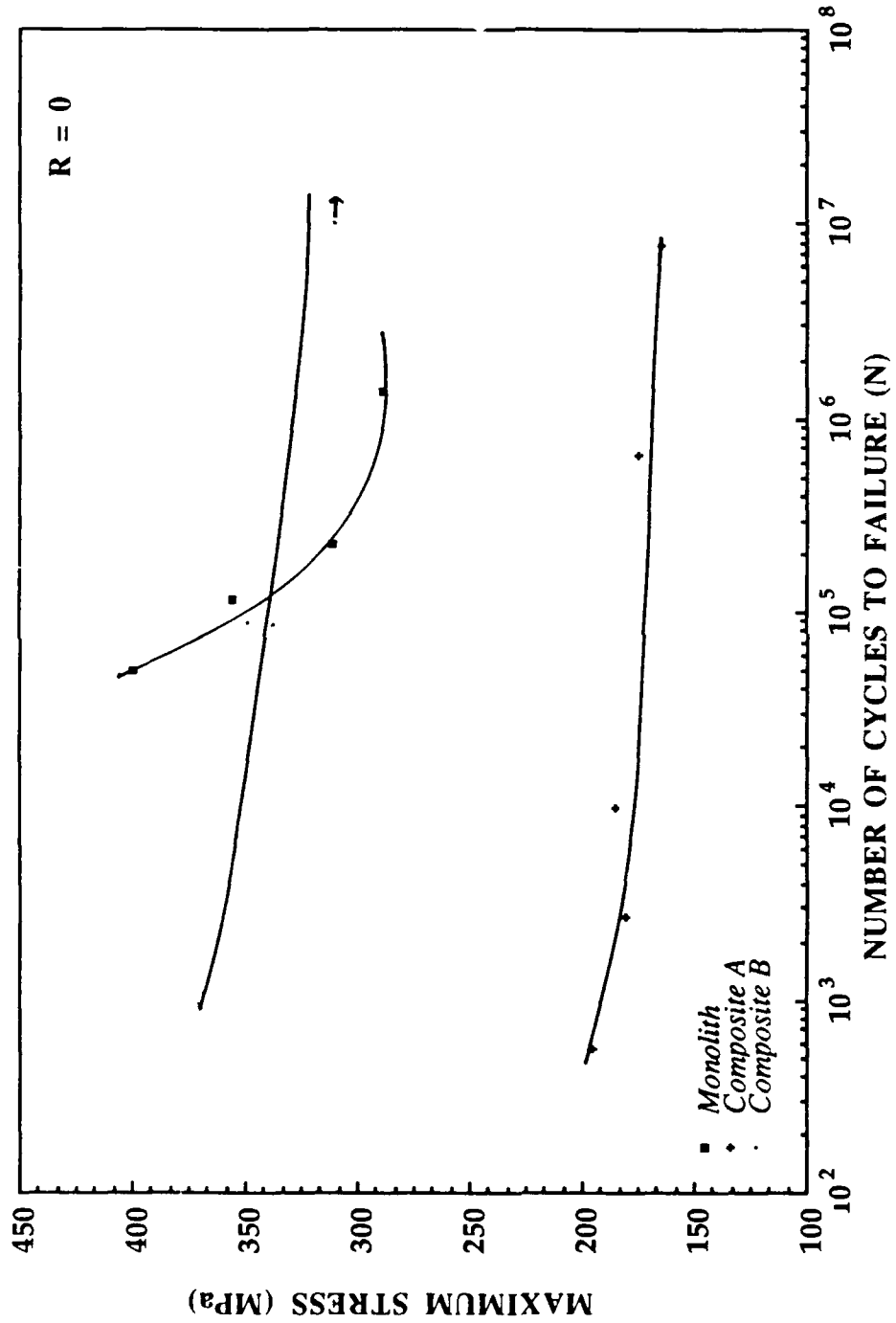


Figure 22: S-N curves for all three specimens using maximum stress values.



Figure 23: Macroscopic view of crack produced in composite A. The arrow indicates the crack initiation site. Magnification = 50X.

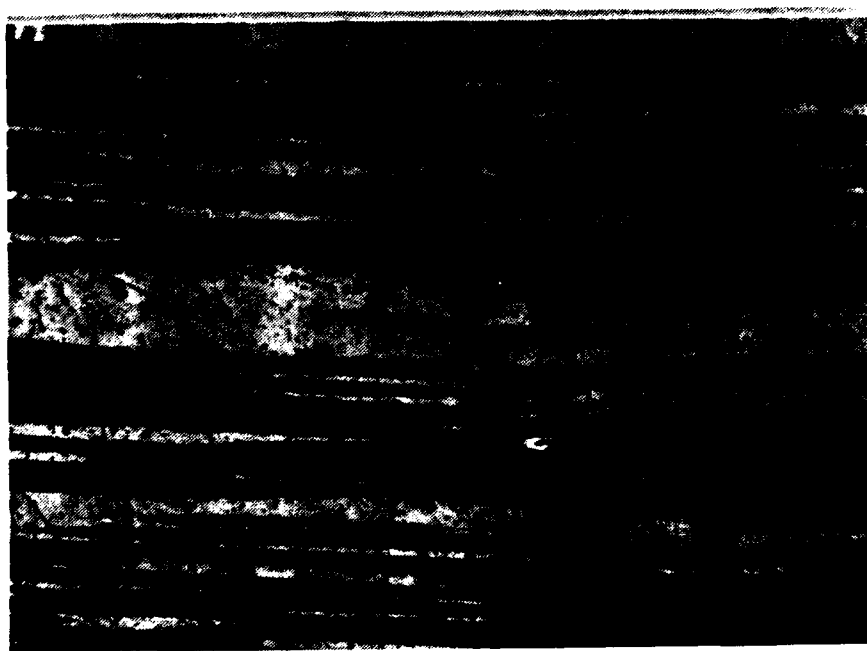


Figure 24: Micrograph of composite A showing fiber buckling and no debonding in the longitudinal layer. This figure corresponds to region X in figure 23. Magnification = 200X.

In the transverse fiber layer (tensile layer for composite A) the crack propagation mechanism is different. Here the crack cleaves the fibers longitudinally, along its basal planes (the P100 Thorne has a radial distribution of basal planes). The basal planes are weakly bonded to each other allowing for easy cleavage along these planes. This is evidenced from figure 25 (also an optical micrograph of composite A), which is a magnified view from figure 23, showing partial cross sections of fibers.

For composite B, optical micrographs of the crack shown in figures 26 and 27 reveal tremendous necking of the matrix in the tensile layer. Very little fiber/matrix debonding is seen, as noted from figure 27, which is a magnified view of the tensile loaded ply in figure 26. Figure 28 shows the central transverse ply for composite B, and some fiber cracking along the basal planes can also be seen.

Finally, some fiber buckling can be seen in the compressive side of the sample in figure 26 (region Z).

Based on the optical micrographs, figures 23 to 28, and the secant modulus versus number of cycles plot, figure 20, the mechanisms of crack propagation for the two composite orientations can be determined. Composite B has a longer fatigue life than composite A at all stress levels; the reason is inherent in the favorably oriented "crack divider" orientation of the outer most ply of composite B. Most of the fatigue crack propagation life is spent here. As the crack moves inwards, it encounters the transverse layer that provides little resistance to its motion. In composite A the center fiber layer is longitudinal and in the favorable "crack divider" orientation, however, by the time the crack has reached the central ply, the increased crack length, stress concentrations and

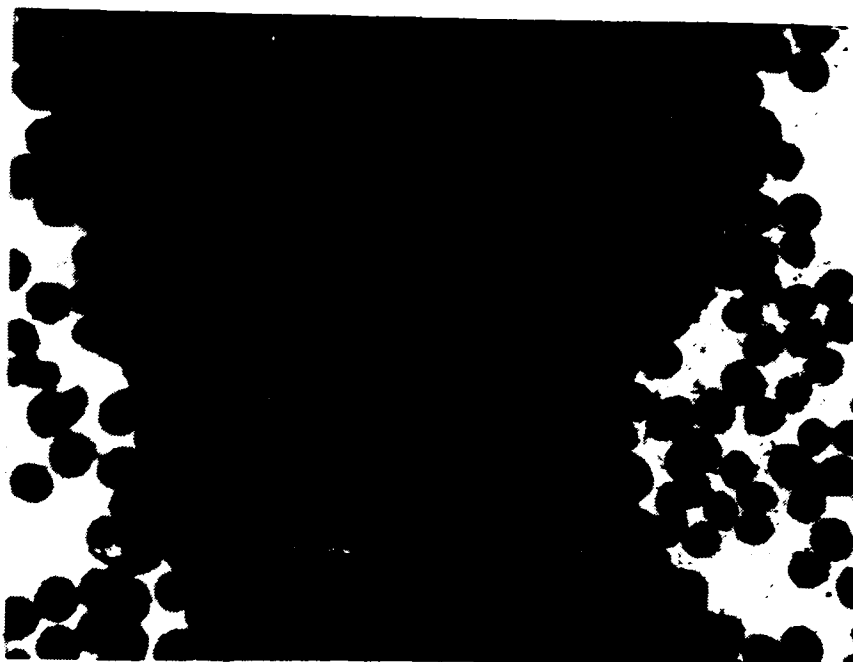


Figure 25: Micrograph of composite A showing the weak basal planes of the graphite fibers; evidenced by fiber cracking. This figure corresponds to region Y of figure 23. Magnification = 500X.



Figure 26: Macroscopic view of the crack produced in composite B which reveals tremendous necking of the matrix. Magnification = 50X.



Figure 27: Micrograph of composite B showing little fiber/matrix debonding. This figure corresponds to region X of figure 26. Magnification = 200X.



Figure 28: Micrograph of composite B showing some fiber cracking along the basal planes in the transverse plies. This figure corresponds to region Y of figure 26. Magnification = 500X.

higher stress levels (since the fatigue is load controlled) reduce the longitudinal fibers' ability to act as a crack inhibitor.

From these initial studies, the following conclusions can be drawn for bend fatigue testing of P100 Gr/6061 Al, [0/90] cross ply composites:

Crack initiation:

- Initiation does not necessarily occur at the outside surface (the region of maximum applied tensile stress).
- Initiation is heavily aided by manufacturing flaws, leading to initiation inside the composite. Poor infiltration due to fiber clustering leads to voids which are the primary crack initiation sites.

Crack propagation:

- If fibers are oriented perpendicular to the crack front, the crack can split the fiber and propagate through, or propagate around the fiber (i.e., "crack divider" orientation).
- If fibers are oriented parallel to the crack front, propagation can either debond the interface and propagate around the fiber or split the fiber along a plane parallel to its basal plane orientations and propagate through the fiber.
- Longitudinal fibers are the most effective crack propagation inhibitors. However, in bending fatigue, the longitudinal fiber's ability to inhibit crack propagation decreases as crack length increases.

General fatigue behavior:

- A distinct endurance limit exists in fatigue for the composite samples.
- No clear cut region corresponding to stress and strain controlled fatigue exists in the composites.

- The S-N curves of the composites are much shallower than that of the monolith (i.e., a large increase in fatigue life with a small drop in stress level). This is typical for composites since the larger number of obstacles in the crack path become more effective crack growth inhibitors with a decrease in stress level.
- Since the fatigue life in both composites is crack propagation controlled, the composites are considered to be notch insensitive.

VI. SUMMARY

A diffusion bonded [0/90] cross ply 6061-P100 Al-Gr composite has been tested in thermally cycled conditions. The large fiber volume ($\geq 40\%$) gave poor liquid metal infiltration during the fabrication step and led to possible sites for crack initiation during thermal cycling due to the large residual stresses set up by temperature differences. Interface debonding resulted giving rise to fiber protrusion from the edges as seen in figure 11. The cycling between room temperature and i) 540 °C and ii) 100 °C gave large residual strains after the first cycle. These were tensile in nature and were caused by time dependent plasticity (creep) in the matrix due to the large tensile residual stresses existing in the matrix after fabrication. These tensile residual stresses, in longitudinal plies, reach large values due to the cross plying of these laminate MMCs. Hysteresis also exists between the heating and cooling segments and has been explained by residual stresses either aiding or opposing the natural response of the matrix. It was seen that a stress relief heat treatment at 200 °C followed by quenching to room temperature gave the smallest residual strain after cycling. Finally the interface between the graphite and aluminum showed a dispersed coating of TiB. No carbides were found, even after cycling up to 540 °C for 72 cycles.

The two factors important for explaining hysteresis and residual strains are as follows:

- The residual stress state of the matrix after fabrication.
- The matrix time dependent plastic response at elevated temperatures.

A cast [0/90] cross ply 6061-P100 Al-Gr composite using two different orientations has been tested in load controlled bend fatigue conditions. The large fiber volume (40%) again caused poor liquid infiltration that led to reduced strength and stiffness in bending. Secant modulii of the composites and monolith revealed that the composites' fatigue failure is crack propagation controlled and the monolith is crack initiation controlled.

S-N curves showed composite A to have poor fatigue properties in relationship to composite B and the monolith. The monolith has the best fatigue properties at low cycles while composite B is the best choice for high cycle fatigue.

Microscopy showed crack initiation to occur inside the surface. Fiber cracking due to basal plane orientation was seen in both composites. An improvement would involve a fiber with an "onion peel" design to reorient the basal planes.

Fiber orientation has a definite effect on the fatigue life of these Al-Gr composites. Fatigue life depends heavily on the orientation of the outer most ply (with the longitudinal orientation giving the highest resistance to crack growth). As the crack propagates, stress concentration and increased stress levels, reduce the effectiveness of a favorably oriented longitudinal layer in the interior of the sample.

APPENDIX A

The dilatometer was set-up and operated as per the operation instructions.

The thermocouple used in the dilatometer is platinum-platinum/10% rhodium. The thermocouple's response is non-linear, therefore, writing a program to collect temperature data was difficult.

The basic equation used to convert millivolts to temperature is shown below.

$$\text{millivolts} = A + BT + CT^2 \quad (6)$$

A, B, and C are constants and T is temperature in °C. Values for A, B, and C were determined using published values of the thermocouple's output at various temperatures. Six equations were developed to cover from 0 °C to 500 °C in 100 °C increments.

The dilatometer was then operated using the computer program to measure the temperature to determine where multiplying factors were needed to ensure the temperatures being generated by the computer were within 1 °C of the actual temperature; a copy of the program is included at the end of this appendix.

In order for the acquisition unit to extract the proper data, the "T Range" dial on the dilatometer must be set to 1500 °C and the "Expansion Multiplier" set to 0.2. The leads from the acquisition unit are to be connected to the leads that run from the dilatometer

to the plotter. The plotter and acquisition unit should be used together. The plotter data was used to ensure proper data was being extracted by the computer.

To start, load the sample into the dilatometer and make adjustments as per the operation manual; do not push "run" yet. Run the computer program to extract data every second and print it to the screen. If the temperature on the dilatometer and the computer is approximately the same, then the leads are connected properly. Let the program run for about a minute then write down the average of the expansion, Ex, in millivolts. Stop the program so you can edit the "Y" variable to equal the average value for expansion, line 55 of the program, and set the print statement to send the data to the printer. This zero's the displacement in percent inches (i.e., actual displacement = value from computer/100) for the start of the run and gives a hardcopy of the data. Press "run" on the dilatometer and restart the program; taking data every three minutes was sufficient for our test.

When the run is complete, shut off the dilatometer, stop the program and analyze the data, interpolate as necessary.

The manufacturer of the dilatometer recommends a heating rate of 1 °C or less per minute when heating to temperatures below 300 °C. Once the temperature is past 300 °C, the heating rate can be increased.

When cooling, it is necessary to cool at a rate of about 1 °C every 3 - 4 minutes when the temperature is below 200 °C. This is due to the mass of the furnace.

The program is shown on the following two pages.

```

10 ! Program to read data from the dilatometer.
20 ! Written 05-09-90 by Kellogg/Hansen.
30 ! Revised May 11, 1990.
31 ! T range switch on the dilatometer must be set for 1500 C.
40 DIM Temp(5001), Extens(5001)
50 T_start=0
51 INPUT "Is the T range switch set for 1500 C (1 = yes)?",X
52 INPUT " Is the expansion multiplier set for 0.2 (1 = yes)?",Xx
54 INPUT "Specify interval between readings, sec",W
55 Y=0.000
57 T_end=W*5000
70 T_total=T_end-T_start
71 T_0=TIMEDATE
80 OUTPUT 709,"CLR"
90 OUTPUT 709;"USE 000"
100 OFF KEY
110 PRINTER IS 701
120 FOR I=0 TO 5000
130 REPEAT
140 T_i=(TIMEDATE-T_0)
150 UNTIL T_i>=(T_total/5001)*(I)
151 OUTPUT 709;"CONFMEAS DCV, 212"
152 ENTER 709;Extens(I)
160 OUTPUT 709; "CONFMEAS DCV, 214"
170 ENTER 709; Tmv
180 IF Tmv<= 0.00032 THEN
190 Tem=Tmv*1000*1.35
191 END IF
192 IF Tmv. 0.0032 THEN
193 Tem=Tmv*1000*1.425
194 END IF
195 IF Tmv>0.000377 THEN
196 Tem=Tmv*1000*1.44
197 END IF
198 IF Tmv>0.00045 THEN
199 Tem=Tmv*1000*1.46
200 END IF
202 IF Tmv>0.000536 THEN
203 Tem=Tmv*1000*1.485
204 END IF
205 IF Tmv>0.0007 THEN
206 Tem=Tmv*1000*1.55
207 END IF
208 IF Tmv>0.0010306 THEN

```

```

209  Tem=Tev*1000*1.6
210  END IF
211  IF Tmv>0.001349 THEN
212  Tem=Tmv*1000* 1.623
213  END IF
214  IF Tmv>0.00199999 THEN
215  Tem=Tmv*1000*1.634
216  END IF
217  IF Tem<= 0.645 THEN
218  Temp(I)=-293.0851+SQRT(343595.5186+425531.92*Tem)/2
219  END IF
220  IF Tem>0.645 THEN
221  Temp(I)=-569.4974+
SQRT(1138.9948*1138.9948+4*(6953.1129+181143.012*Tem))/2
222  END IF
223  IF Tem>1.42 THEN
224  Temp(I)=-1089.33997+
SQRT(2178.67993*2178.67993+4*(39301.554+303186.5*Tem))/2
225  END IF
226  IF Tem>2.323 THEN
227  Temp(I)=-1810.7164+
SQRT(3621.43284*3621.43284+4*(105298.52+461041.96*Tem))/2
228  END IF
229  IF Tem>3.26 THEN
230  Temp(I)=-2842.327+
SQRT(5684.654*5684.654+4*(231740.473+675675.676*Tem))/2
231  END IF
232  IF Tem>4.234 THEN
233  Temp(I)=-3577.845+
SQRT(7155.68997*7155.68997+4*(346742.98+822386.42*Tem))/2
234  END IF
235  Ext=0.01*(Extens(I)-Y)/0.0009652
237 PRINT USING
"4D,2X,3A,2X,DD.4D,X,2A,2X,2A,X,3D.DD,2X,3A,X,DD.7D,X,A,2X,2D.5D,X,2A";I,
"Temp";Temp;"mV","C=",Temp(I),"Ex=";Extens(I),"V",Ext;"in"
238 NEXT I
239 END

```

APPENDIX B

Replicas taken of the edges of the thermally cycled composite were produced using the following procedure.

First, one edge of the samples was polished using 1 μm diamond paste and marked so the same edge would be used for all replicas for accurate comparison.

Three pieces of thick acetate tape were cut approximately 1.5 inches long. The tape was handled with tweezers to prevent finger prints from contaminating the replicas. A clean, glass slide was used as a flat, smooth surface. With the tape on the slide, the prepared edge of the sample was sprayed with acetone, the excess shaken off, and pressed firmly on to the tape. Caution must be taken to ensure the sample does not shift on the tape until the acetone has evaporated. Once the acetone had evaporated, the tape was peeled off the sample and set in a clean, dry area. Each replica was examined under an optical microscope to check their quality. Three replicas of the edge were taken each time to increase the chances that at least one was free of bubbles.

After the replicas were inspected, the bad ones were thrown out. If all were bad, new replicas were made. The good replicas were then placed into a vacuum chamber to be coated with chromium using chemical vapor deposition. The replicas were placed in the chamber with the replica side facing up. The tape was coated to better reflect light from the microscope.

After the replicas were coated, the best one was chosen and mounted on a glass slide to help preserve it and to improve microscopy inspections.

LIST OF REFERENCES

1. Rossi, R. C., Pepper, R. T., Upp, J. W., and Riley, W. C., "Development of Aluminum-Graphite Composites," *American Ceramic Society Bulletin*, v. 50, no. 5, pp. 484-487, May 1971.
2. Kural, M. H. and Min, B. K., "The Effects of Matrix Plasticity on the Thermal Deformation of Continuous Fiber Graphite/Metal Composites," *Journal of Composite Materials*, v. 18, pp. 519-520, November 1984.
3. Meyerer, W., Kizer, D., Paprocki, S., Paul, H., "Versatility of Graphite-Aluminum Composites," *2nd International Conference on Composite Materials (ICCM 2)*, pp. 141-152, 1978.
4. Dutta, I., "Thermal Fatigue of P100 Gr - 6061 Al Composite," Progress Report #2 to NWSC Crane, Indiana, April 30, 1990.
5. Tsai, S., Mahulikar, D., Marcus, H. L., "Residual Stress Measurements on Al-Graphite Composites Using X-ray Diffraction," *Materials Science and Engineering*, v. 47, no. 2, pp. 145-149, February 1981.
6. Park, H. S., *Residual Stress Measurement and Microstructural Characterization of Graphite Aluminum Metal Matrix Composites*, PhD Dissertation, University of Texas at Austin, August 1989.
7. Koss, D. A., and Copley, S. M., *Metallurgical Transaction*, v. 2, pp. 1557, March 1971.
8. Garmong, G., "Elastic-Plastic Analysis of Deformation Induced by Thermal Stress in Eutectic Composites: I. Theory," *Metallurgical Transactions*, v. 5, pp. 2183-2190, October 1974.
9. Wolff, E. G., Min, B. K., Kural, M. H., "Thermal Cycling of a Unidirectional Graphite-Magnesium Composite," *Journal of Material Science*, v. 20, pp. 1141, 1984.
10. National Aeronautics and Space Administration Technical Paper - 2612, *Effects of Thermal Cycling on Graphite-Fiber-Reinforced 6061 Aluminum*, by G. A. Dries and S. S. Tompkins, p. 7, October 1986.
11. Dries, G. A. and Tompkins, S. S., Development of Stable Composites of Graphite-Reinforced Aluminum and Magnesium, 12th Conference on Composite Materials and Structures,DOD/NASA Cocoa Beach, Fl., January 20-21, 1988.

12. Khan, I.H., "The Effect of Thermal Exposure on the Properties of Aluminum-Graphite Composites," *Metallurgical Transactions A*, v. 7A, pp. 1281-1289, September 1976.
13. Olsen, G. C., and Tompkins, S. S., "Continuous and Cyclic Thermal Exposure Induced Degradation in Boron Reinforced 6061 Aluminum Composites," *Failure Modes in Composites IV*, pp. 1-21, 1979.
14. Hertzberg, R. W., *Deformation and Fracture Mechanics of Engineering Materials*, 2d ed., pp. 469-477, John Wiley and Sons, Inc., 1983.
15. Stinchcomb, W. W., Reifsnider, K. L., Yeung, P., and Masters, J.. "Effects of Ply Constraint on Fatigue Damage Development in Composite Material Laminates," *Fatigue of Fibrous Composite Materials*, ASTM STP 723, American Society for Testing and Materials, 1981, pp. 64-84.
16. Bhatt, R. T., and Grimes, H. H., "Fatigue Behavior of SiC Reinforced Ti (6Al-4V) at 650 °C," *Metallurgical Transactions A*, v. 13A, pp. 1933-1938, November 1982.
17. Reifsnider, K. L., and Jamison, R., "Fracture of Fatigue-loaded Composite Laminates," *International Journal of Fatigue*, v. 6, n. 4, pp. 187-197, October 1982.
18. Nayeb-Hashemi, H., and Seyyedi, J., "Study of the Interface and its Effect on Mechanical Properties of Continuous Graphite Fiber-Reinforced 201 Aluminum," *Metallurgical Transactions A*, v. 20A, n. 4, pp. 727-739, April 1989.
19. Dvorak, G. J., and Johnson, W. S., "Fatigue of Metal Matrix Composites," *International Journal of Fracture*, v. 16, n. 6, pp. 585-607, December 6, 1980.
20. National Aeronautics and Space Administration Technical Paper - 2701, *The Effects of Thermal Cycling on Thermal Expansion and Mechanical Properties of Several Aluminum Metal-Matrix Composites*, by G. A. Dries and S. S. Tompkins, July 1987.
21. Mallick, P. K., *Fiber-Reinforced Composites*, pp. 91, Marcel Dekker, Inc., 1988.

INITIAL DISTRIBUTION LIST

	No. Copies
1. Defense Technical Information Center Cameron Station Alexandria, Virginia 22304 - 6145	2
2. Library, Code 52 Naval Postgraduate School Monterey, California 93943 - 5002	2
3. Professor I. Dutta, Code ME/DU Department of Mechanical Engineering Naval Postgraduate School Monterey, California 93943 - 5004	2
4. Research Administration, Code 012 Naval Postgraduate School Monterey, California 93943 - 5000	1
5. Robert Hansen 2707 Creekside Drive Newark, Delaware 19711	2
6. Department Chairman, Code ME/HY Department of Mechanical Engineering Naval Postgraduate School Monterey, California 93943 - 5000	1
7. Naval Engineering Curricular Office, Code 34 Naval Postgraduate School Monterey, California 93943 - 5000	1
8. Professor S. Mitra, Code ME/MT Department of Mechanical Engineering Naval Postgraduate School Monterey, California 93943 - 5004	2

- | | |
|------------------------------------------------------------------------------------------------------------------|---|
| 9. Kevin G. Beasley
Naval Weapons Support Center
Electronic Development Department
Crane, Indiana 47522 | 1 |
| 10. Alan S. Edelstein, Code 6371
Naval Research Laboratory
Washington, D.C. 20375 - 5000 | 1 |